Comet 19P/Borrelly at Multiple Apparitions: Seasonal Variations in Gas Production and Dust Morphology

David G. Schleicher, Laura M. Woodney, and Robert L. Millis

Lowell Observatory
1400 W. Mars Hill Road
Flagstaff, Arizona 86001

Accepted by *Icarus*, 8 November 2002

The Lowell Observatory Preprint Series

Comet 19P/Borrelly at Multiple Apparitions: Seasonal Variations in Gas Production and Dust Morphology

David G. Schleicher, Laura M. Woodney, and Robert L. Millis
Lowell Observatory, 1400 W. Mars Hill Road, Flagstaff, Arizona 86001
phone (928) 774-3358, fax (928) 774-6294
E-mail: dgs@lowell.edu; woodney@lowell.edu; rlm@lowell.edu

ABSTRACT

We present analysis and results from both narrowband photometry and CCD imaging of Comet 19P/Borrelly from multiple apparitions. Production rates for Borrelly a few days prior to the Deep Space 1 spacecraft encounter were Q(OH) = 2.1×10^{28} molecule s^{-1}, Q(CN) = 5.1×10^{25} molecule s^{-1}, and $A(\theta)f\rho$ = 400-500 cm. The equivalent Q(water; vectorial) = 2.5×10^{28} molecule s^{-1}. We also find that the radial fall-off of the dust is significantly steeper than the canonical $1/\rho$ for aperture sizes larger than $\rho = 2\times10^4$ km. In the near-UV, a strong trend in dust colors with aperture size is present. Imaging of Borrelly revealed a strong radial jet in the near-sunward direction which turns off late in the apparition. For the jet to appear radial, it must originate at or very close to the nucleus' pole. Modeling the measured position angle of this jet as a function of time during the 1994 and 2001 apparitions yields a nucleus in a simple, rather than complex, rotational state with a pole orientation having an obliquity of 102.°7±0.°5 and an orbital longitude of the pole of 146±1°, corresponding to an RA of 214.°1 and a Declination of –5.°7 (J2000). There is also evidence for a small (~8°) precession of the pole over the past century, based on our preferred model solution for jet measurements obtained during the 1911-1932 apparitions. Our solution for the orientation of the rotation axis implies a very strong seasonal effect as the source region for the jet moves from summer to winter. This change in solar illumination quantitatively explains both the nearly level water production measured in the seven weeks preceding perihelion and the extremely large decrease in water production (25×) as Borrelly moved from perihelion to 1.9 AU. A much smaller fall-off in apparent dust production after perihelion can be explained by a population of old, very slowly moving large grains released near peak water production, and therefore not indicative of the actual on-going release of dust grains late in the apparition. Based on the water vaporization rate, the source region has an area of approximately 3.5 km^2 or 4% of the total surface area of the nucleus, and water ice having an effective depth of 3-10 m is released each apparition from this source region.

Key Words: Borrelly, comets, coma, jets, photometry

I. INTRODUCTION

Discovered at the end of 1904, Comet 19P/Borrelly was observed on five consecutive apparitions before a perturbation of its orbit by Jupiter resulted in very poor observing geometry on the following 6 orbits (cf. Sekanina 1979). Prior to the last of these poor apparitions, another perturbation reduced its orbital period

sufficiently from 7.0 years so that the most recent 4 apparitions have again been relatively favorable, with the best occurring in 1988. Since its discovery, perihelion distances have varied between 1.32 and 1.45 AU; the smallest of these was in 1981, while the most recent 3 apparitions have had a slightly larger value of about 1.36 AU.

Long known to display a persistent, sunward-pointing fan, Sekanina (1979) modeled the orientation of this fan from the 1911 to 1932 apparitions to derive an orientation of the rotation axis. More recently, Fulle *et al.* (1997) analyzed imaging obtained during the 1994/95 apparition with two models, one of which yielded a precessing nucleus. A rotational lightcurve of the nucleus was obtained in late November 1994 by Lamy *et al.* (1998) using the Hubble Space Telescope (HST); these data implied that Borrelly's nucleus was very elongated and rotated with a period of 25.0±0.5 hr. In 2000, Mueller and Samarasinha (2002) obtained a period of 26.0±1 hr when the comet was at r_H = 3.8 AU. In addition, during the past two decades a variety of other investigators have examined relative and absolute gas production rates (Q) in the visible (Newburn and Spinrad 1984; Boehnhardt *et al.* 1989; Meredith *et al.* 1989; Cochran and Barker 1999) and dust properties in the thermal IR (Hanner *et al.* 1996; Li and Greenberg 1998) . Most recently, Borrelly became the focus of numerous observing campaigns because of the planned fly-by of the comet on 2001 September 22 by the Deep Space 1 (DS1) spacecraft. The encounter was very successful, resulting in only the second comet nucleus to be imaged from up-close, revealing a very dark, elongated body with several narrow jets emanating from a relatively small region near the presumed pole (Soderblom *et al.* 2001; Soderblom *et al.* 2002).

As part of our long-term photometry program begun by A'Hearn and Millis (A'Hearn *et al.* 1979; A'Hearn and Millis 1980), Borrelly was observed in 1981, 1987/88, and 1994/95. Analysis of observations from the first two apparitions as a part of our database indicated that Borrelly is slightly depleted in carbon-chain molecules, and that its Q(OH) r_H-dependence after perihelion was the steepest of any of the 85 comets contained in our database (A'Hearn *et al.* 1995). In late 1988, we also attempted to measure rotational lightcurves of the nucleus in the visible and thermal IR, in the same manner as we had previously successfully employed for comets such as 49P/Arend-Rigaux (Millis *et al.* 1988) and 10P/Tempel 2 (A'Hearn *et al.* 1989). Unfortunately, all of the nights when simultaneous visible and IR measurements were scheduled were clouded out, and the only night when visible photometry was obtained clearly showed that the nucleus signal was overwhelmed by the coma.

Given this background, we planned our 2001/02 observing campaign with several goals in mind. First, we wished to expand our heliocentric distance coverage of the comet both before and after perihelion, in order to improve our determination of the r_H-dependence in the production of gas and dust. Second, these same observations plus associated imaging observations would place the extremely brief DS1 encounter observations into a broader context. Third, we hoped to determine gas and dust production rates just prior to the encounter to assist the last-minute observing plans of other investigators for the encounter; our efforts were successful and our results were immediately disseminated to the community (Schleicher 2001). Fourth, we hoped that imaging of the jet(s) in Borrelly's coma would allow us to constrain the pole orientation and the location of the source region(s) on the nucleus, and to investigate whether or not the steep r_H-dependence of the production rates was due to seasonal effects resulting from the changing latitude of the sub-solar point

with orbital position. In this paper, we report results relating to each of these goals. In addition, we also investigate the evolution of the color and spatial distribution of the dust and the apparent change in dust-to-gas ratio during each apparition, and look for evolutionary changes from apparition to apparition.

II. OBSERVATIONS AND REDUCTIONS

Instrumentation

All observations, except for one night, were obtained with the Perkins 72-inch (1.8-m), the Hall 42-inch (1.1-m), or the 31-inch (0.8-m) telescopes located at Lowell Observatory. The remaining night of photometry (1987 December 24) was obtained at the University of Hawaii's 88-inch (2.2-m) telescope at Mauna Kea Observatory. The same photoelectric photometer with pulse counting electronics was used for all photometric measurements during Borrelly's first three apparitions. This system was replaced with a new photometer for the most recent apparition, but with the same phototube and electronics. All imaging was obtained at the Hall 42-inch, using a Loral 800^2 CCD in 1994/95 and a SITe 2048^2 in 2001/02. On-chip, 2×2 binning resulted in final pixel scales of 0.72 and 1.13 arcsec, respectively.

Three different epochs of narrowband comet filters have been used in our Borrelly observations: the original A'Hearn and Millis set was used in 1981, the International Halley Watch (IHW) set plus the older NH filter in 1987/88 and 1994/95, and the new HB set in 2001/02 (cf. Farnham *et al*. 2000, and references therein). These filters isolate the emission bands of OH, NH, CN, C_3, and C_2, and continuum points in the near-UV and blue-green regions of the spectrum. Note that the location of the UV continuum filter has changed from 3675 to 3650 to 3448 Å as we changed from the original filter set to later versions. Similarly, the green continuum location has changed from 5240 to 4845 to 5260 Å. The new HB set has an additional (blue) continuum filter at 4450 Å, permitting additional color measurements to be obtained. A subset of image quality versions of these filters was used in the CCD observations, as well as a broadband CalTech R filter, having a nearly square 2600 Å bandpass centered at 7000 Å, in 1994/95, and a broadband Kron-Cousins R filter in 2001/02.

CCD Observations and Reductions

Because Borrelly was not particularily bright, the "R" band filters were used for the majority of the imaging, and a subset of the narrowband filters was used only on some of the nights. On these few, good-quality nights, photometric standards were also imaged. Exposure times for Borrelly ranged from 30 to 600 s for the broadband images, and up to 600 s for the CN filter. Observational parameters for the 11 nights of imaging are summarized in Table I; two other nights of imaging in 1995 May are not included because the data had insufficient signal-to-noise (S/N) to be of use in these investigations.

Mean bias and flat frames were determined for each night and applied to the comet and standard star frames. Photometric frames discussed in this paper were flux calibrated, and continuum images were scaled and subtracted from the emission band images using our standard photometric procedures (cf. Farnham *et al*. 2000). Centroiding was performed by fitting a 2-D parabola to the apparent photo-center in each image;

because the inner-most coma is dominated by dust, this was adequate for registration even among images obtained through various filters. Borrelly's nucleus was not detected. The 2-D parabola was first fit to a region of 30 by 30 pixels to obtain the approximate center, then refit to a 5 by 5 pixel region, essentially the peak of the effective seeing profile. Our estimated uncertainty in centering is 0.5 pixels, which is dominated by the possible offsets caused by the jet and tail morphology.

To improve the contrast of morphological features such as the sunward jet, the relatively benign azimuthal median division image enhancement technique we have previously used (cf. Schleicher and Woodney 2002) was applied. In brief, a median image is produced from the images obtained with a specific filter on a single night and the azimuthal median profile is extracted. This profile is then used to create a synthetic image which is divided into each of the original frames. This process has the effect of removing the bulk radial profile but enhancing any azimuthal asymmetries or morphological features such as jets. Moreover, the positions of the jets are unchanged, which is not the case for some other enhancement techniques such as unsharp masking or rotational shift differencing. An example of this processing is shown in Figure 1, where representative dust and CN images are presented before and after image enhancement. Finally, in order to measure precisely the position and width of Borrelly's sunward jet as a function of time and distance from the nucleus, we also "unwrapped" the *x-y* images, producing θ-ρ figures from which the position and width of the jet could easily be extracted. These figures will be discussed further in Section V.

Photometry Observations

Photometric observations were obtained following our usual procedures (cf. A'Hearn *et al*. 1995): An individual data set typically consisted of several 10-30 s integrations with each filter using a circular entrance aperture centered on the comet, along with associated sky measurements >0.25 degrees away. Projected apertures varied from 5 to 199 arcsec in diameter due to differing instrumentation and specific observing goals during these four apparitions. Measurements of comet flux standard stars were made over a range of airmass to provide nightly extinction coefficients and instrumental calibrations for each filter, which were subsequently used to reduce the comet observations to absolute fluxes above the atmosphere.

A total of 118 photometric sets were obtained during 29 nights of observations. Observational parameters such as heliocentric distance (r_H), geocentric distance (Δ), phase angle, and time from perihelion are given in Table II for each night. Heliocentric distances range from a preperihelion value of 1.47 AU to a smallest perihelion value (1981) of 1.32 AU and up to a maximum distance following perihelion of 1.89 AU. The time of observation from perihelion (ΔT) varies from –50 to +120 day; data have been obtained within 9 days of perihelion at each apparition. On several nights during the 1987/88 and 1994/95 apparitions, most measurements were obtained through a relatively small aperture to investigate possible rotational variability. These monitoring data have been closely examined and although in a few instances a small trend through the night was detected, no clear rotational signature was evident. Therefore, we have averaged all data obtained with a particular aperture on each night to improve the S/N and to avoid overweighting these nights in the subsequent analyses, resulting in 74 averaged sets. The aperture diameters in arcseconds and the log of the projected radius (ρ) in kilometers are given in Table III, along with the number of photometric measurements averaged together.

Photometry Reductions

Although the basic methodology used to reduce the photometry to continuum and emission fluxes is the same as discussed in detail in A'Hearn *et al*. (1995), several specific procedures have recently been revised with the introduction of the new HB filter set (Farnham *et al*. 2000). These procedures include improved decontamination of the continuum filter measurements from the wings of the C_2 and C_3 emission bands, improved continuum subtraction from the gas filter measurements, better determination of the non-linear extinction of the OH band in the near-UV, and revised fractional band transmission coefficients for C_2 and C_3. Equivalent new procedures and coefficients were also determined for the previous filter sets, and these have been employed in the current reductions. Due to a degradation of the transmission of the original NH filter with age, the fraction of the NH emission band (3360 Å) transmitted by the filter has slowly decreased over time. Measurements of the filter are consistent with a near-constant rate of degradation, and appropriate correction factors of about 1.06, 1.35, and 1.64× have been applied to the NH measurements from 1981, 1988/89, and 1994/95, respectively. The resulting emission band and continuum fluxes are listed in Table III, with averages from multiple apertures within a night listed in order from largest to smallest aperture.

Further reductions to column abundances and production rates for the gas species and to the quantity $A(\theta)f\rho$, a measure of dust production, follow our standard procedures and use the coefficients detailed in A'Hearn *et al*. (1995). In brief, theoretical fluorescence efficiencies (L/N) are used to compute the number of molecules contained within the photometer entrance aperture. For OH, NH, and CN, L/N varies with heliocentric velocity ($\dot{r}_H$) and, in the case of CN, heliocentric distance. Therefore, these nightly L/N values are also listed in Table II. The column abundances, $M(\rho)$, are then extrapolated to total coma abundances using a standard Haser model, followed by the computation of production rates (Q) by dividing the total coma abundances by the assumed lifetime of each observed species (see Table III). Resulting gas production rates will be independent of aperture size if the Haser model scalelengths accurately reproduce the radial distribution of the gas species. Our measure of dust production, $A(\theta)f\rho$, is the product of the dust albedo at a particular phase angle with the filling factor and the projected aperture radius. This quantity, first introduced by A'Hearn *et al*. (1984), will be independent of aperture size if the dust follows a canonical $1/\rho$ radial distribution, and independent of wavelength if the dust is grey in color. Gas and dust production rates are given in Table IV.

Of the observed gas species, only OH has a single parent species, H_2O, and adequately determined lifetimes and velocities to permit the computation of parent production rates. We again use the empirical relation determined by Cochran and Schleicher (1992) to convert from the Haser model OH production rate to a vectorial equivalent water production rate (also see A'Hearn *et al*. 1995 and Schleicher *et al*. 1998b); these are also listed in Table IV. While our production rate computations do not include the effects on gas species' lifetimes due to changing solar activity, we discuss these effects in Section III.

The uncertainties shown in the various figures and listed in Table IV are based on photon statistics for single data points, but when more than one point has been averaged together within a night, the uncertainty is from the RMS scatter among the points.

III. PRODUCTION RATES

Heliocentric Distance Dependence

We begin our analysis by examining the gas and dust production rates as a function of the heliocentric distance (r_H); the logarithm of each quantity is plotted in Figure 2. Each apparition is distinguished with a different symbol, and observations obtained prior to perihelion are shown as filled symbols. As is evident from Figure 2 and Tables II-IV, our temporal coverage is much more extensive after perihelion, and unweighted linear least-squares fits (dashed lines) are therefore only presented for the post-perihelion data. Because the perihelion distance in 1981 was significantly smaller than at subsequent apparitions, the 1981 data were not included in these fits; if they had been included, the resulting slopes would have been even steeper than described below. Examination of the coefficients of the fits, listed in Table V, reveals the exceptionally steep drop in gas production rates. As already noted in the introduction, the r_H-dependence for OH of –8.9 is the steepest of any comet in our database (A'Hearn *et al*. 1995), and the other gas species have similarly steep slopes. (Note that two abnormally low NH measurements were excluded from the fit which is shown and tabulated; if these points were included, the slope would be –12.0.) To emphasize the magnitude of this behavior, note that production rates might be expected to decrease by approximately a factor of 2-3 between 1.36 AU and 1.89 AU due to the change in solar radiation, whereas Q(OH) instead decreased by ~25×. Interestingly, these results for the gas species contrast sharply with the r_H-dependence of $A(\theta)f\rho$ at each continuum wavelength, all of which have power-law slopes near –3. Our explanation for this large difference between the gaseous species and the dust will be discussed in Section VI.

Although the range of r_H sampled before perihelion is too small to compute meaningful r_H-dependencies, it is evident from Figure 2 that the gas production rates are systematically higher before perihelion than after perihelion over the same distances. This is particularly obvious for the carbon-bearing species. Again, the dust exhibits a different behavior from the gas, apparently having no asymmetry about perihelion.

It is somewhat difficult to directly intercompare absolute production rates from one apparition to another both because of the effects of changing solar activity and differences in the projected aperture sizes. The strongest trends with aperture size are evident for $A(\theta)f\rho$, and these will be discussed in detail in Section IV. Occasional trends in production rates with aperture size are also evident within individual nights for certain gas species, particularly for CN and C_3 in 1987 at low solar activity (see Table IV), but almost no trends are visible for the gas species in 2001 close to solar maximum. We conclude that the Haser model scalelengths we have used generally provide a good approximation for the spatial distributions of the gas, particularly near solar maximum. We attribute some of the apparent differences between apparitions to changes in solar activity and the resulting changes in lifetimes of parent and daughter species. For instance, the derived production rates of OH, CN, and C_2 from observations obtained a few days after perihelion in 2001 are noticeably higher than those obtained in 1987 and 1994. To approximate the effects of the expected increase in water and OH lifetimes at solar minimum; (cf. Cochran and Schleicher 1993), a sample calculation for OH was performed using a Haser parent scalelength 50% longer and a daughter scalelength and lifetime 20% longer than our canonical values. The resulting OH production rate was approximately 25-30% higher,

almost exactly accounting for the apparent discrepancy between 1994 and 2001. A similar test for CN also largely removes the offset, and so we conclude that apparent differences between apparitions can be mostly attributed to solar activity. Therefore, we see no evidence of significant evolutionary trends in absolute gas production rates with apparition, except for 1981, when the perihelion distance was significantly smaller than for later apparitions. Moreover, as is also evident from Figure 2, the steep post-perihelion r_H-dependence in each species' gas production repeats every orbit. This fact alone provides strong evidence that the steep fall-off with heliocentric distance following perihelion *cannot* be due to the exhaustion of volatiles on the surface of the nucleus.

Composition

The relative abundances, as defined by the average ratio of production rates, are listed in Table V. All measurements were included in the computation of these unweighted mean values. As expected from the similarity in the gas r_H-dependencies, there is very little trend in the relative gas abundances with heliocentric distance. Because of our improved understanding of the filter coefficients and the extent of the wings of the C_2 and C_3 emission bands (see Farnham *et al*. 2000), a comparison of Borrelly's abundance ratios with the taxonomic classes in the A'Hearn *et al*. (1995) database must be made with caution. In particular, the change in the adopted C_3 band shape affects the UV continuum determination, which in turn affects the continuum subtraction. As discussed recently by Schleicher and Osip (2002), on average the improved calibration coefficients result in slightly decreased CN band fluxes (~7%), slightly increased C_2 (~10%), but a very large (2.1×) increase in C_3. While each of these adjustment factors will vary somewhat with the particular gas-to-dust ratio of each comet, to first-order *all* comets will be similarly affected when reduced with the same calibration coefficients and, therefore, intercomparisons between comets using the same coefficients will be largely unchanged. In the future, the entire photometric database will be reanalyzed with the improved coefficients.

Independent of whether or not one adjusts values for other comets, the log of the production rate ratio for C_2-to-CN, –0.29, clearly places Borrelly into the carbon-chain depleted classification of A'Hearn *et al*. (1995). Using the adjustments for CN and C_2 just discussed, we would expect that the mean "typical" value would be approximately 0.13, and that Borrelly's C_2-to-CN ratio is about 2.6× below this mean typical value. Not unexpectedly, given the comet's consistency from apparition to apparition, this degree of depletion is essentially identical to that obtained by A'Hearn *et al*. based only on the 1981 and 1988 apparitions.

As usual, comparisons of our results with those of other researchers are complicated by the usage of differing fluorescence efficiencies and/or model scalelengths and lifetimes. The easiest comparison can be made with the spectroscopic results from Farnham and Cochran (2002), who adopted our scalelengths in their analysis because of the generally good match to the spatial profiles of the gas species. While our absolute production rates are systematically higher than theirs, we have confirmed that this is primarily due to the spatial asymmetries for the gas species coupled with the differences in fluorescence efficiencies used by the two groups. Derived abundance ratios are the same to within the uncertainties.

Previously, Cochran and Barker (1999) had analyzed their extensive set of spectroscopic measurements from the 1981, 1988, and 1994 apparitions, also concluding that Borrelly is depleted in carbon-chain molecules. While Cochran and collaborators and ourselves have the only large compositional datasets for Borrelly, several other groups have more limited data sets, including Newburn and Spinrad (1984), Boehnhardt *et al*. (1989), and Williams *et al*. (1990). Even though Newburn and Spinrad used significantly different model parameters than ourselves, they noted that Borrelly's C_2-to-CN ratio is much lower than most comets in their database. Additional discussion of the various abundance ratio determinations is given by Cochran and Barker.

Water production

Vectorial-equivalent water production rates are listed in the final column of Table IV, based on our Haser-model OH production rates as indicated in Section II. Because the conversion includes an $r_H^{-0.5}$, the post-perihelion r_H -dependence for water is steeper by this factor, resulting in a power-law slope of –9.44. We will return to the cause of this exceptionally steep slope in Section VI.

We are aware of only two other determinations of the OH production rate. One was obtained by Bockelée-Morvan *et al*. (1995) from radio measurements in 1994 between Sept 20 and Oct 11. Their value, 2.4×10^{28} molecules s^{-1}, is in excellent agreement with our values for the corresponding time before perihelion in the last three apparitions. The other OH measurements are from Cochran and Barker (1999), which were also obtained during the 1994 apparition. As they noted, their results were about a factor of 10 lower than the summary results given in A'Hearn *et al*. (1995). As a test, Cochran (personal communication) has computed production rates using our model parameters and has confirmed that their CN and C_2 production rates are essentially identical to ours on two nights when the comet was observed simultaneously by the two groups. However, the use of identical model parameters for OH still results in more than a 4× discrepancy, which Cochran now believes was primarily due to problems with their flux calibration in the UV.

IV. DUST CHARACTERISTICS

In addition to the relatively shallow r_H -dependence exhibited by the dust as compared to any of the measured gas species, we indicated that significant trends with aperture size were evident in the photometric data. Before examining these aperture dependencies and the associated radial profiles of the dust, we note that effects due to changing phase angle for the dust can easily be eliminated as a source for any of the characteristics of the dust discussed here. In particular, all of the photometric measurements were obtained between phase angles of 29 and 45 degrees, a region over which the phase function is nearly flat (cf. Hanner and Newburn 1989; Gustafson and Kolokolova 1999), and only the images obtained late in each apparition ($r_H > 2$ AU) had somewhat smaller phase angles. Phase effects are, therefore, essentially negligible (≤10%) for these data, and we have not applied any correction for phase angle to the derived $A(\theta)f\rho$ values.

Because of the large difference in r_H-dependencies for the dust and the gas, the derived dust-to-gas ratio for Borrelly obviously greatly varies during each apparition. Using the unweighted average of all observations, as measured by $\log A(\theta)f\rho/Q(\mathrm{OH})$ in units of cm s $\mathrm{molecule}^{-1}$ in the green continuum, the dust-to-gas ratio

was –25.40±0.31. This value is near the middle for all comets measured in the A'Hearn *et al*. (1995) database. If only observations obtained at $r_H < 1.45$ AU are included, the ratio drops to –25.6, while it increases to –24.9 if only the data obtained beyond 1.8 AU are used. This large variation will be examined further in Section VI.

Spatial Distribution of Dust

To investigate trends in $A(\theta)f\rho$ with aperture size, we plot in Figure 3 the relative log $A(\theta)f\rho$ as a function of log ρ for all nights for which log ρ varies by at least 0.2. Different observing runs are distinguished by alternating open and shaded symbols; all adjacent measurements having the same symbol were obtained over a time span of 3 days or less, minimizing possible changes due to comet variability. Each data set has been normalized using a linear fit for log r_H vs log $A(\theta)f\rho$ having a slope of –3 and an intercept of 3.05, and additionally shifted vertically based on the time from perihelion (right-hand axis labels). All uncertainties are smaller than the plotted symbols. It is immediately evident that the derived value for $A(\theta)f\rho$ nearly always decreases with increasing ρ. When a sufficient range of ρ was measured, it is also evident that the rate of decrease accelerates at large log ρ. These can be compared to the expected constant value for $A(\theta)f\rho$ if the radial profile of the dust followed a canonical $1/\rho$ distribution. There is also evidence that the slopes are steepest early in each apparition, and become more level late in the apparition. Unfortunately, differences in geocentric distances and instrumentation meant different ranges of log ρ were measured in the 1987 and 2001 apparitions, preventing us from directly comparing the two apparitions. In fact, the combination of these effects is the cause for the smaller value for the post-perihelion r_H-dependence of the blue continuum as compared to the UV and green continuum given in Table V — no small aperture observations were obtained with the blue continuum filter, which was only used during the 2001 apparition.

We can also extract the equivalent information directly from our narrowband imaging. As an example, we have performed a series of aperture extractions from the green continuum images obtained on 2001 September 22, the only photometric night close in time to our photoelectric data and, coincidentally, only 12 hr prior to the DS1 encounter. These extractions are shown as the solid curve in the right-hand panel of Figure 3. The extractions show a relatively constant $A(\theta)f\rho$ for apertures smaller than 2.5×10^4 km, consistent with the canonical $1/\rho$ fall-off for the dust, while a much steeper fall-off occurs beyond 4×10^4 km.

Because, of course, successively sized apertures include all of the flux from the smaller apertures, the effects of a departure in the radial distribution of dust from a canonical $1/\rho$ fall-off are diluted in $A(\theta)f\rho$ values. Radial profiles obviously provide a more direct measure of the dust fall-off, and CCD images also allow us to examine the fall-off in different directions, such as along the jet and the tail, separately from the general, ambient coma. However, signal-to-noise constraints require us to use the wide R-band filter, rather than the narrowband comet filters for this aspect of the investigation. Because most nights of imaging were non-photometric, and the wideband images are uncalibrated in any case, all images from an individual night were averaged before normalized profiles were extracted.

In Figure 4 we show radial profiles along the jet, tail, and the ambient coma. The jet and tail profiles are medians of a 20° wedge centered on the measured jet location and centered in the anti-solar direction,

respectively. The ambient coma profile is derived from the average of two 90° median profiles, each centered perpendicular to the sun-tail line. In the case of 2002 January 12, a special region had to be defined to extract an ambient profile because the jet remnant contaminated one of the standard ambient regions. In this case we used a single 120° wedge centered on a PA of 44°. The inner cutoff for the radial profiles is at 7.5 arcsec. This is 2.5 times the average seeing during the observations (as determined from the FWHM of the standard stars observed). The outer cutoff is determined by the distance at which the signal in the profile of the ambient coma region has dropped to three times the uncertainty in the sky measurement. In some cases, residual gradients across the chip due to poor quality twilight flats significantly increased the sky uncertainty, requiring us to truncate the profiles at smaller projected distances than usual.

Examining Figure 4, it is immediately evident that the profile which consistently best matches a canonical $1/\rho$ is the one extracted in the anti-solar direction, i.e., the dust tail. In comparison, the ambient coma profiles also follow a $1/\rho$ slope out to $1.0\text{-}1.5\times10^4$ km, but progressively become steeper beyond this distance. As shown by Baum *et al.* (1992) and references therein, this behavior is just what would be expected for non-fading grains affected by radiation pressure. In the perpendicular direction, as radiation pressure effects begin to dominate, more dust grains are swept away than are replaced, leading to a departure from $1/\rho$. Baum *et al.* showed this effect became significant at about 10^5 km when they assumed an outflow velocity (v) of 1 km s^{-1}. Moreover, the distance to which particles travel before radiation pressure dominates their motion is proportional to v^2. Therefore, the observed distance in Borrelly at which the departure from $1/\rho$ becomes apparent corresponds to an outflow velocity of about 0.4 km s^{-1}, consistent with numerous estimates for dust outflow velocities. In the tail direction, Baum *et al.* demonstrated that non-fading grains should produce a $1/\rho$ profile *independent* of the particle size distribution or original outflow velocity, again consistent with the tail profile we observe in Borrelly.

As expected, the radial profile of the jet is brighter than profiles in other directions early in the apparition. What was not expected was that the jet's profile approximately followed a $1/\rho$ falloff to beyond 3×10^4 km near perihelion, and to at least 4×10^4 km late in the apparition, well beyond the turn-down observed for the ambient coma. While it is tempting to suggest that the dust grains in the jet had a significantly higher velocity than the ambient coma, this solution would not explain other attributes of the jet. For instance, if we compare the jet's profile to the ambient coma, it is evident that the peak relative brightness slowly progressed outward during the apparition — just the opposite expected with the change in viewing geometry. (Note that bumps in the jet profile on September 20 centered at $\log \rho = 4.3$ and 4.7 are artifacts caused by star trails; the September 22 and 23 profiles better represent the jet's behavior in this time frame.) Overall, these results from the CCD radial profiles are consistent with our conclusions based on the aperture photometry, i.e. that the distance at which the dust profiles depart from $1/\rho$ progressively increases throughout the apparition. We will return to the jet's evolution with time in Section VI.

Dust Colors

We begin our analysis of the color of the dust grains by simply plotting the differences in $\log A(\theta)f\rho$ values between pairs of continuum filters in our photometry. These are shown, as a function of heliocentric distance, in Figure 5. While the dust is clearly reddened for each of these continuum pairs, there is no trend

in the amount of reddening with r_H. The relatively large amount of scatter in the top and bottom panels is partly due to the relatively poor S/N in the ultraviolet, as indicated by the sometimes large error bars. Another source of scatter in the bottom panel is caused by different baselines for the green and UV continuum locations among the different filter sets. However, the most interesting source of scatter is due to a significant trend of colors with aperture size. These aperture effects are shown in Figure 6, where we plot the measured reflectivity for the blue and UV continuum, normalized to each filter set's green continuum, as a function of log ρ. In the UV, the lowest reflectivity, i.e. largest reddening, occurs for apertures smaller than about 1×10^4 km, and the grains approach solar colors with progressively larger aperture sizes. In contrast, no obvious trend is evident for the blue continuum, but a smaller range of aperture sizes was measured.

While the change in continuum wavelengths among the different filter sets is a nuisance when intercomparing colors for the various baseline pairs, we can use these different continuum points to our advantage when plotting the reflectivities as a function of wavelength, as shown in Figure 7. To minimize scatter caused by lower S/N data, we have limited this analysis to data taken at $r_H < 1.45$ AU, noting that we had already shown that the dust colors were independent of heliocentric distance. Here, we first computed reflectivities normalized to the green continuum, but then have renormalized observations obtained with the IHW filters to compensate for this set's green continuum location at 4845 Å, rather than at 5240 or 5260 Å used in 1981 and 2001, respectively. To determine the appropriate amount of adjustment, we computed the mean reflectivity at the HB blue continuum location of 4450 Å, which was 0.87. Because the IHW 4845 Å filter is slightly less than half-way between 4450 and 5260 A, we assigned it a reflectivity of 0.93 and accordingly reduced all of the associated IHW 3650 Å filter reflectivities by 7%.

Because of the strong trends in the UV reflectivity as a function of aperture size, we also averaged the data into 5 aperture bins, separated at 1×10^4, 2×10^4, 4×10^4, and 8×10^4 km, and these bin averages are shown with differently sized symbols. To distinguish the error bars associated with each averaged value, we have also slightly off-set the UV and blue data points in wavelength. It is apparent that if only intermediate aperture sizes are considered, such as $1\text{-}4\times10^4$ km, the reflectivity can be approximated by a linear fit over this range of wavelengths, as is shown by the dashed line. This fit corresponds to a reddening of 17% per 1000 Å. This degree of reddening is near the high end of measurements in the visible region of the spectrum (Jewitt and Meech 1986) and is most similar to the 18% per 1000 Å measured by Jewitt and Meech for Comet C/Shoemaker (1984s) at a similar heliocentric distance.

We can compare these reflectivities to mean values extracted from the CCD narrowband imaging from 2001 September 22 as a function of projected distance, ρ. In these data, no obvious trend of the color with ρ is apparent out to distances where S/N requires us to truncate the data, i.e., $\rho = 2.5\times10^4$ at the blue continuum and 4×10^4 km in the red (7128 Å). The derived reflectivities, again normalized to green continuum, are shown in Figure 7. Most importantly, the CCD data provide a measure of the reflectivity in the red, greatly extending the wavelength coverage. The derived values at the red continuum point clearly indicate that the reddening of the grains observed in the UV and blue regions of the spectrum extends out to the near-IR. This extension of the reddening out into the near-IR likely requires a significant population of relatively large-sized grains, i.e. larger than several microns (cf. Gustafson and Kolokolova 1999). This contrasts with

earlier results for Comet Hyakutake (1996 B2) by Schleicher and Osip (2002), where the dust colors were strongly reddened at short wavelengths, but were grey in color beyond about 6000 Å, implying a somewhat smaller average grain size than for Borrelly.

We also attempted to extract dust colors as a function of location within the coma from the narrowband CCD imaging. There is some indication that the reflectivity at 4450 Å is closer to solar at $\rho > 1\times10^4$ km along the jet than at similar distances in the tailward or ambient coma directions. Using the longer baseline of the blue and red continuum filters, a similar result is obtained. Although the overall scatter in the measurements makes this result inconclusive, we can compare our measured reflectivity of the dust to the results obtained by Farnham and Cochran (2002) using long slit spectra. Conveniently, they also normalize the reflectivity to their green continuum location of 5245 Å. Overall, their optocenter measurements show the least reddening, opposite of the general trend we measured with aperture size; however, we never measured apertures comparable in size with their optocenter extraction, so it is possible that dust in the inner-most coma is greyer in color. Their extractions along the slit at differing orientations near perihelion imply that the sunward jet is greyer in color than either the ambient coma or the tail, consistent with our tentative finding beyond 10^4 km.

V. DUST JET MORPHOLOGY AND MODELING

A persistent, relatively narrow sunward fan has been reported for Comet Borrelly since its 1911 apparition (eg. van Biesbroeck 1914; Sekanina 1979). More quantitative measurements at visible and near-IR wavelengths in recent years of the narrowness of this feature (Lamy *et al*. 1998; Fulle *et al*. 1997) implied that it must emanate from a relatively localized source region on the nucleus; hence, we use the term "jet" to distinguish it from a much broader sunward fan which would originate from a uniformly volatile surface. And unlike the spiral jets observed by numerous investigators in Comets Hale-Bopp (1995 O1) and Hyakutake (1996 B2), Borrelly's jet is nearly linear in appearance and exhibits little or no motion from night-to-night, implying that the source must be located close to or at the rotational pole. Note that the corresponding CN jet is quite broad in comparison (Figure 1), as might be expected due to the additional dispersion resulting from the dissociation of parent molecules.

Jet morphology in 2001/02

To examine the dust jet's morphology in more detail, we first applied azimuthal median division image enhancement to each image, described in Section II. From the resulting *x-y* images, it is evident that the relative strengths of the jet and the tail vary through the apparition, with the jet weakening over time (Figure 8). The apparent distance of the peak relative brightness with respect to the surrounding coma increases through the apparition, from a projected distance of less than 10^4 km in September, to about 3.2×10^4 km in November and 3.6×10^4 km in December. Slight curvature of the jet is also evident in December, qualitatively consistent with radiation pressure effects as the direction of the jet began to diverge from the projected direction of the sun. By January, a feature at a PA of about 140° appears to be residual, slow-moving material associated with the jet, but detached from the inner-most coma and nucleus and distorted due to radiation pressure and projection effects. Finally, in March the coma structure becomes much more

amorphous, with the tail no longer clearly evident and the strongest feature being a curved jet on the western side. A very faint, diffuse feature is also visible (with suitable enhancements and stretches) in the south-east quadrant of the March images, which we identify as the persistent remnant jet. The new jet towards the west is apparently the same feature identified by Farnham and Cochran (2002) in their February and May images, and we discuss it further at the end of this section.

By progressively overlaying a radial line at differing position angles (PAs), we visually determined a single, best value of the PA of the sunward jet on each frame from September through December. These were then used to compute a mean value for each night, which are listed in Table VI as $PA_{x\text{-}y}$. We also "unwrapped" the enhanced images, creating θ-ρ plots, from which we could more readily quantitatively examine the jet's physical characteristics (note that θ represents the position angle, and should not be confused with the phase angle in $A(\theta)f\rho$). Examples are shown in Figure 9. These were created with a 1° resolution in the θ direction, while binning to 4× the original pixel scale in the ρ direction. To further reduce the pixel-to-pixel variations due to noise, these were then smoothed with an 11-pixel boxcar in the theta direction. Finally, intensity plots were then extracted at each binned position of ρ between approximately 10 and 40 arcsec, from which the position and value of the peak intensity and half-power points could be determined.

From these measurements, we see no evidence of any variations which might be caused by rotation, such as a corkscrew appearance or changes in PA during a night or from night-to-night. Instead, all variations in the measured PAs appear to be random, typically <1-2 pixels, and are consistent with level of noise in the images. The accuracy with which we were able to extract the location of the peak brightness along the jet varied with distance and date. In particular, uncertainties in the original centroiding could result in errors in the extracted position angle of up to 4° at a distance of 10 arcsec, but only 1° at 40 arcsec. Fortunately, this source of uncertainty is random, and is reduced by averaging the results from multiple frames from a given night. In November and December, the jet's contrast with the background is very low inside of about 20 arcsec, resulting in a very broad peak; we considered giving these measurements a lower weight in our averages, but as this did not affect the final values, we continued to weight all measurements from the θ-ρ intensity plots equally. We did, however, extend our extractions on these nights to one additional 4 pixel bin in ρ to partially compensate for the change in spatial scales due to the decrease in geocentric distance.

In all, 6 or 7 measurements of the jet were determined between about 10 and 40 (or 44) arcsec for nearly all θ-ρ plots, on 2-7 frames per night. The mean PA for each night from this technique is listed in Table VI as as $PA_{\theta\text{-}\rho}$. In combination with the mean values directly extracted from the *x*-*y* images described earlier, a final, adopted value for the position angle of the jet (PA_{jet}) is also listed, rounded to the whole degree. We can estimate an uncertainty for each night based on the scatter among the individual measurements, the apparent noise, and the number of images. We have also checked our fundamental coordinate system, by computing the plate solution for numerous standard star frames taken on these nights. On average, the *y*-axis of the CCD chip is rotated from north by 0.°7, and this offset has been accounted for in all of our measurements. We also found that the direction of north can vary by about 0.°1 as a function of position in the sky or filter, presumably due to possible instrument flexure, differential refraction, or deviations of the filter mounting to the normal direction. Combining these sources of uncertainty, we conclude that our

absolute results for Sept 22 and 23, and Nov 20 are each better than 0.°5, while Sept 20 and Dec 6 are better than 1°.

Remarkably, the width of the jet, as characterized by the FWHM compared to the ambient coma, is essentially constant with distance beyond about 20 arcsec. Our mean values for the FWHM are 36° in September, 38° in November, and 42° in December, with uncertainties of 1, 2, and 3°, respectively. The September value is completely consistent with the value of 35° measured independently by both Samarsinha and Mueller (2002) and Farnham and Cochran (2002). A slight asymmetry in brightness and width is also visible in the sides of the jet, particularly close to the nucleus, with the counterclockwise side (i.e. larger PAs) being brighter.

Because the jet is relatively narrow, very straight (except for expected radiation pressure effects seen in December), and shows no rotational modulation, we conclude that the peak brightness along the jet must also follow along the projected rotational axis of Borrelly's nucleus. Note that we do not require the source region to be exactly centered on the pole of the nucleus, but simply sufficiently close (perhaps within 5°), to minimize a corkscrew morphology. One might imagine a source region 15° in radius from which dust emanates with sufficient dispersion to have a 36° FWHM jet. If the source were centered at a latitude of 85°, the maximum expected variation of the PA of the peak brightness of the jet (and the edge locations) with rotation would be 10°, but this would expected to be dampened due to a range of grain velocities. For the claimed 25 hr rotation period (Lamy *et al*. 1998) and an assumed dust outflow velocity of 0.4 km s^{-1} (from Section IV), our chosen range of ρ for extractions covers an entire rotation cycle. In any case, by fitting over a sufficently large range of ρ on different dates, any corkscrew-type characteristics will be averaged out and, when the pole is continually illuminated — as we show later — the rotationally averaged peak brightness will be directly *along* the axis, rather than centered on the middle of the source region.

Modeling the jet and pole solution

In order to reproduce the observed jet morphology as a function of date, we have utilized the 3-D Monte Carlo jet model created by Farnham and Schleicher (Schleicher *et al*. 1998a; Farnham *et al*. 1999) for Comet Hale-Bopp, and recently used by Schleicher and Woodney (2002) to model the dust jets in Comet Hyakutake. In brief, this model permits us to place extended source regions on the surface of a nucleus, which release particles as a function of solar illumination. While these calculations are performed in the comet's orbital reference frame, a series of transformations are applied to create the view of the comet as seen from Earth (see Schleicher and Woodney 2002 for details). Because of Borrelly's extremely simple jet morphology — essentially a radial jet centered along the projected rotation axis — most of the complications involved in fitting the model to observations could be avoided. In particular, a small source can be placed exactly at the pole to produce the linear jet, eliminating the need to conduct a search of the latitude and longitude parameter space, as well as other parameters such as dust velocity, degree of dispersion, and rotation period. Instead, one only needs to search a two-dimensional parameter space defined by the obliquity of the rotation axis and the orbital longitude of the pole, which define the 3-D orientation of the rotation axis. In this case, a grid pattern search can be performed to determine a series of viable solutions at each date of observation. Each series corresponds to a great circle defined by the plane containing the

viewer (i.e. Earth), the nucleus, and the projected jet on the sky. With each change in viewing geometry, a new series of viable solutions is obtained, and the intersection of solutions from different nights will correspond to the physical orientation of the rotation axis.

Two caveats must be noted. First, we assume that the nucleus is not experiencing complex rotation, but is instead in a state of simple, principle axis rotation, and the rotation axis is identical to the angular momentum vector. This assumption can be checked by intercomparing the solutions from different nights and even different apparitions. Second, even with simple rotation, two diametrically opposite solutions are actually determined from this process. Since initially there was no clear evidence for whether Borrelly is in prograde or retrograde rotation, we arbitrarily assigned the solution pointing nearest to the sun at perihelion as the north pole and our quoted orientations are for this pole.

For practical purposes, given the relative uncertainties and overall consistency between the measured nightly averages for Sept 20, 22, and 23 (see Table VI), we grouped these three together as if we had one highly accurate measurement of 94° on the 22nd. This was combined in our model fitting with a slightly more uncertain value of 120° on Nov 20, and the least accurate value, but still with an uncertainty of <1°, of 132° for Dec 6. This resulted in three crossing points or solutions, one for each pair of dates. These three solutions varied by less than 1° in obliquity, but by a total of 6° in orbital longitude. However, when the associated uncertainties are included, a single overall solution containing each measurement is obtained, having an obliquity of 102.°7±0.°5 and an orbital longitude of the pole of 147±2°. It should be noted that, by chance, on Nov 20 the uncertainty in the measured PA directly corresponds to an equivalent change in the pole obliquity, and that this night's data provide almost no constraint on the orbital longitude of the pole. Therefore, the orbital longitude is only constrained by the September and December measurements. Our pole solution can be readily transformed to the equivalent standard celestial equatorial coordinate system, with $\alpha = 214.°8$ and $\delta = -6.°3$.

Our solution for the pole orientation can be directly compared to those obtained by Farnham and Cochran (2002) and Samarasinha and Mueller (2002) for the 2001/02 apparition. In particular, we differ from the Farnham and Cochran result by 1° in obliquity and 2° in orbital longitude, well within their quoted uncertainties. While we differ by a larger amount, 6°, from the center of a family of solutions by Samarasinha and Mueller, their solution set is only well constrained in 1 dimension, and their swath of solutions in fact passes only 0.5° from our value. A comparison with the pole solution from the DS1 observations will be made in Section VII.

Pole Orientation in 1994/95

The excellent agreement between the strongly constrained solutions by Farnham and Cochran and ourselves over a nearly 3-month interval in 2001 gave us strong reason to believe that Borrelly is, indeed, in simple rotation with a stable pole orientation. In contrast, Fulle *et al.* (1997) proposed two possible model solutions to reproduce the jet orientation extracted from a compilation of images obtained during the 1994/95 apparition. They claimed they either needed an outburst which released very low velocity particles at one time, or a more steady-state release of grains from a precessing pole. As a test of their results and our own

model, we used our solution from 2001/02 to predict the expected PA of the jet on the date and time of each of their tabulated measurements. As we discuss in detail later in this section, except for one datum obtained late in the 1994/95 apparition after we would expect the source to have shut down, our predictions were in excellent agreement with the tabulated measurements by Fulle *et al.*, confirming our simple rotation model without significant precession.

To further test and constrain our solution for the pole orientation, we also measured representative images we obtained early in the 1994/95 apparition, in the 6-week interval prior to the beginning of the Fulle *et al.* data set. This interval has a range of ΔT of –48 to –25 day, corresponding to more than a month before our earliest imaging during 2001/02. Using the same measurement method as for 2001, our averaged results for the polar jet are again listed in Table VI; a rotation of the *y*-axis of the Loral CCD chip from north by about 1°.5 has been accounted for in these measurements. In addition to sampling a different portion of Borrelly's orbit, these data more tightly constrain the orbital longitude of the pole than was possible in 2001/02 due to the particular observing geometries. The 1994 September data in particular require an orbital longitude of 1-2° smaller than the value of 147°(±2°) determined for 2001; however, a decrease of 2° or more begins to yield systematic offsets for both our 2001 data and Fulle *et al.*'s 1994 data. Taken together, we concluded that a 1° decrease in the orbital longitude of the pole gave the best overall fit for both apparitions, i.e. an obliquity of 102°.7±0°.5 and orbital longitude of 146±1°. This result corresponds to $\alpha = 214°.1$ and $\delta = -5°.7$ (J2000). We do not quote uncertainties for the RA and Declination because while the associated error ellipse has the same size as in the comet's reference frame, the error ellipse is rotated to an oblique angle in the equatorial coordinate system.

Our preferred pole solution for the combined 1994/95 and 2001/02 apparitions is used to compute the sub-Solar and sub-Earth latitudes, as well as the predicted position angles of the jet ($PA_{94/95}$) in Tables VI and VII. As can be seen from Table VI, the average difference between the measured jet PA and the model is less than 1°. In the case of the Fulle *et al.* measurements listed in Table VII, our predicted PAs are within 5° of each of their measurements except for their final image and, excluding this measurement, our average difference in PA is only 1°.7. Moreover, their final image was obtained on 1995 March 11, 130 days past perihelion. This corresponds to a time following our detection during the current apparition of what appears to be a detached, remnant jet distorted by radiation pressure, and additional evidence for this scenario will be discussed in Section VI. We, therefore, suggest that the position angle measured by Fulle *et al.* from their final image — which is very diffuse in any case — does not represent the extension of the polar axis, and so should not be used when constraining the pole orientation. We suspect that it was Fulle *et al.*'s need to match the measurement from this final image which led to their large precession solution.

Pole Orientation in 1911-1932

Given the stability of the orientation of the spin axis in the two most recent apparitions, it is reasonable to ask if the pole orientation was the same a century ago. Although Borrelly has undergone several orbital perturbations by Jupiter, these have all taken place at much larger distances from Jupiter than would be required to affect its rotational spin state (cf. Scheeres *et al.* 2000), and so the orientation of the spin axis should remain invariant except for torques introduced by non-gravitational effects. With the primary source

region located at or very close to the pole, one would also expect such torques to be small in size, and the non-gravitational force to be nearly constant from apparition to apparition.

Sekanina (1979) modeled an ensemble of reported positions of the sunward fan from the 1911/12 to 1932/33 apparitions (van Biesbroeck 1914, 1920, 1927, 1934; Chofardet 1913; Jeffers 1926) to determine both a pole orientation and direction of rotation for Borrelly, along with three other comets. In this analysis, Sekanina determined the difference in the PA of the sunward feature to that of the PA of the Sun, and interpreted any difference as simply resulting from thermal phase lags coupled with viewing geometry of the solar insolation on an isotropic surface. In other words, by assuming that a thermal phase lag caused a peak emission at the same time in the local "afternoon," a pole solution could be computed from observations at differing viewing geometries.

However, the existence of jets emanating from isolated source regions in Comet 1P/Halley (cf. Keller *et al.* 1988), coupled with multiple narrow jets observed in a variety of comets, has led to the more recent understanding that most comets are not uniformly volatile over their entire surface. If one or more isolated source regions are present, then the orientation of the jet does not in and of itself provide a constraint on the thermal phase lags, and the direction of rotation can only be determined by modeling the shape of the jet. For Borrelly, an isolated active region (or multiple sub-regions) clearly causes the observed morphology, as evidenced by the narrowness of the jet as seen both from groundbased and DS1 images.

For these reasons, we must conclude that the assumptions made by Sekanina, while reasonable at the time, are invalid, as is any pole solution based on these assumptions. We, therefore, attempted a basic reanalysis of these early measurements, in light of our current understanding of the nature of the sunward feature. Unfortunately, many of the recorded descriptions of the coma morphology in the early 20th century are somewhat ambiguous. For instance, van Biesbroeck (1920; 1927; 1934) (or a translator) often appears to indiscriminately use the term "tail" to describe the brightest feature, even if it is pointing in the sunward direction. Therefore, we first grouped the potentially useful measurements based on the original descriptions and the associated viewing geometries. We began by separating out measurements of the true tail, using the known anti-solar direction. This group contains all of the measurements Sekanina listed in his Table V for the "late" tail, as well as measurements obtained earlier in the apparition which Sekanina did not tabulate. A comparison of these true tail measurements with the projected anti-solar direction showed that the values usually matched to better than 5-10° until the comet became faint late in an apparition. This provides a simple test of the typical measurement accuracy associated with the data.

After removing observations that were obviously of the true tail, we compiled the remaining measurements and these are listed in Table VII. Note that this group of measurements is identical to the group of data listed in Sekanina's Table IV of the "fan." We next assigned these data to one of three rankings or categories, based on the original published descriptions associated with a measurement. Approximately three-quarters of the data have no ambiguous issues — both the jet and the true tail were reported, or viewing geometry analysis confirms that the reported feature was not the true tail. We assign these measurements of the jet to Category 1. Within Category 2, we place measurements for which an ambiguity remains, because the anti-solar direction is in the same hemisphere as our predicted polar jet. This second group only contains

observations obtained within 10 days of perihelion in 1911, some of which describe the fan as either asymmetric or chevron shaped (Van Biesbroeck 1914; Chofardet 1913). Finally, one observation, from 1911 at ΔT = +26.4 day, was obtained under poor conditions and the feature is described as "vaguely visible"; we assigned this to Category 3, and consider it unreliable. Therefore, while we are in complete agreement with Sekanina as to which observations pertain to the jet, we believe four measurements must be treated with caution and one measurement should probably be discarded. The assigned categories are given as a superscript to the measure position angles, PA_{jet}, in Table VII.

We then proceeded in a manner similar to our analysis of the Fulle *et al.*'s data set from the 1994 apparition, by first utilizing our 1994/2001 pole solution and computing a predicted position angle of the jet for each of these older measurements. Looking first at the Category 1 data, the average difference of the prediction from the observed PA was 11°, and the maximum difference was 23°. However, a clear trend was observed, with nearly all of the predicted PA values being larger than those observed. Moreover, the four Category 2 measurements were offset by 48-69°. While these latter discrepancies might be explained by contamination of the true tail, which varies in PA from 48° to 59°, other factors also contribute. In particular, our 2001 solution implies that the pole, and therefore the jet, should point to within 10° of Earth during the interval just before perihelion in 1911, i.e. the Category 2 points. In this case, even a relatively narrow jet could appear as a very broad fan. Therefore, one could reasonably argue that the combination of a much broader jet caused by viewing geometry, coupled with an overlapping tail, could explain the Category 2 observations.

An alternative scenario, however, is also possible and, we believe, more likely. Note that with the pole pointing almost directly towards Earth, a slight error in the pole orientation can produce a large change in the jet's PA. Since we also detected a trend in the differences for the Category 1 data, we next investigated whether a small change in the pole position might yield a significant improvement in the fit, by varying the obliquity and orbital longitude of the pole. It became apparent that a decrease of about 5-10° in either one or both of these values would remove the overall trends in the Category 1 data. Moreover, within this range of possibilities, a much smaller range of obliquities could also remove the large discrepancies for the Category 2 measurements. Our best solution for the 1911-1932 interval has an obliquity of 96° and orbital longitude of 142°, with an estimated uncertainty of about 2° in each dimension. This solution, corresponding to an RA of 217° and a declination of +2°, reduces our average difference between prediction ($PA_{11/32}$) and observation (PA_{jet}) to less than 8°, including all Categories 1 and 2 data, with no significant trends. This is completely consistent with the general accuracy of individual measurents we found for the true tail measurements. Also, just prior to perihelion in 1911, the jet and the tail would appear to be only about 20° apart, matching the description of a chevron shape. Finally, we checked the results of the analysis by Farnham and Cochran (2002) to confirm that we did not miss other, viable solutions at greatly different pole orientations; in fact, their best solution from a reanalysis of these early apparitions is within a few degrees of our own.

Our preferred solution in these early epochs, more than 30° from Sekanina's solution, directly implies that the sub-Earth latitude peaked at +84° only 6 days before perihelion in 1911, i.e. the jet pointed nearly at the Earth. Also, we would predict that the sub-Solar latitude reached Borrelly's equator approximately 70 days

following perihelion. This is completely consistent with the fact that the latest measurement of the jet in any of these early apparitions occurred at +78 days; following this value for ΔT, only the true tail was measured by the visual observers.

Because this pole solution for these early epochs is only 8° from our 2001 solution (see Table VIII), we can tentatively conclude that Borrelly's rotation axis is slowly precessing by only slightly more than 1/2° per orbital revolution. This slow rate of precession validates our determination of a single pole solution based on data from both the 1994 and 2001 apparitions, as 1/2° is less than our estimated uncertainties. This relatively slow precession rate is quite reasonable given that the bulk of the non-gravitational forces caused by the jet are along the rotation axis (cf. Samarasinha 2002), and that the transverse nongravitational term has been constant over time (Yeomans 1972).

Southern Hemisphere Jet

We previously noted that a weak jet became visible late in the 2001/02 apparition in images obtained both by Farnham and Cochran (2002) and ourselves. Having already tightly constrained the pole orientation for this apparition, we also investigated if we could constrain the location of the source region of this secondary jet, and possibly determine whether the direction of Borrelly's rotation is pro-grade or retro-grade.

From our images from 2002 March 18 and Farnham and Cochran's images from 2002 February 7 and May 17 and 18, it is evident that we are viewing this secondary jet side-on, rather than face-on. The overall shape is similar in each month's images, with the jet emanating from the nucleus towards the northwest and then rapidly curving towards the west. In particular, the initial projected direction of the jet close to the nucleus on March 17 is at a PA only about 7° smaller than the 323° projected orientation of the south pole for this date. Moreover, the jet was also observed to emanate in projected directions within 10° of the pole for each of Farnham and Cochran's images. This would imply that the source of this secondary jet is likely located close to the pole, and possibly within 10° of the pole, consistent with the conclusion by Farnham and Cochran. However, the jet's rapid curvature towards the west is larger than would be expected for a jet located this close to the pole. While Farnham and Cochran suggested the curvature observed in February was caused by radiation pressure, the persistent curvature of the secondary jet towards the west in March and May is inconsistent with the Sun's position angle changing from 71° to 303°. Even with Borrelly's relatively small phase angle (21-23°), radiation pressure effects on micron-sized grains emitted by a near-polar secondary source should have pushed small grains towards the projected anti-solar direction, since the pole orientation remained within about 20-30° of the plane of the sky. Additionally, the secondary jet becomes essentially straight beyond about 8000 km in February and March, but in March this is not in the anti-solar direction.

An alternate source of curvature would, of course, be caused by nucleus rotation. In this case, the source must be located further away from the pole, and the similar shapes observed each month imply that the comet was observed at similar rotational phases. While unlikely, in this scenario the jet shape is more readily reproduced if the sense of rotation matches our original arbitrary assignment of the north pole being in the sunward direction near perihelion. Following the right-hand rule, the Sun illuminated the north pole at

perihelion and, given that the obliquity of the pole is greater than 90°, the direction of rotation is retrograde with respect to Borrelly's orbital motion. However, the linear nature of the jet beyond 8000 km in February and March appears to be inconsistent with a corkscrew shape caused by nucleus rotation.

For these reasons, we instead suggest that the westward extension of the jet may be due to much older, slow-moving grains, either emitted by the secondary source or emitted by the primary source much earlier in the apparition. The possibility that the unusually shaped, and near-constant jet morphology might be caused by the overlap of a near-polar jet and older material is made more viable because the viewing geometry for Borrelly as seen from Earth remains nearly constant throughout the first half of 2002. Unfortunately, this alternate scenario implies that the observed curvature may not be solely caused by cometary rotation, making it much more difficult to ascertain the direction of nucleus rotation. In any case, the analysis of additional images of Borrelly during 2002 would greatly assist in choosing among these different scenarios.

VI. SEASONAL EFFECTS

Although we cannot be sure of how Borrelly appeared to the eye through a telescope a century ago, images obtained from groundbased telescopes, HST, and DS1 at recent apparitions provide a definitive picture: a narrow, radial jet is created from a relatively small source region centered at or very close to the sunward-facing rotational pole near perihelion. Based on the stability of this solution over two apparitions and, with only slight adjustment, over the past century, we can investigate the consequences of this physical scenario. In particular, we have determined several seasonal effects which result as the comet moves along its orbit about the Sun. The first of these is the degree of foreshortening which the jet should exhibit as viewed from Earth. Because the jet is located at the pole, the amount of foreshortening is simply the cosine of the sub-Earth latitude (see Table VI). For a jet of a particular characteristic width, we expect the observed apparent width to increase with the foreshortening, and the widths measured in Section V during 2001 are consistent with this. From foreshortening, one might also expect that the projected distance from the nucleus at which the peak brightness along the jet is located would appear to move closer to the nucleus over the apparition, but we previously showed that the opposite occurs. We will discuss the likely cause of this phenomenon near the end of this section.

Water Vaporization

Looking next at the predicted sub-solar latitude as a function of time as given in the top panel of Figure 10, it is evident that the available solar radiation at the polar source region rapidly declines following perihelion, with the source expected to move into continuous darkness within about +80 to +100 days. Qualitatively, this is very consistent with the decreasing brightness of the jet from month to month as compared to the brightness of the tail. It is also evident from Figure 10 that the sun was highest in the sky as seen from the source region 6 weeks prior to perihelion, when the sub-solar latitude peaked at +77°. Therefore, we expect the peak gas production to have occured between $\Delta T = -43$ and 0 days, when the heliocentric distance was at a minimum, and this can be seen to be true from Figure 11, where we plot production rates as a function of time from perihelion.

To further quantify these seasonal effects, we have computed a theoretical water production curve using a two-component model. The first component is, of course, the polar source region, while the second component is a source producing the residual gas following the shut-down of the polar region late in the apparition. For this purpose, we assume that this secondary source is isotropic over the nucleus, perhaps due to leakage through the crust. However, it might instead be a small, isolated source in the southern hemisphere, associated with the weak second jet observed by Farnham and Cochran (2002) in 2002 February and by ourselves the following month. As we will show, an incorrect assumption regarding the nature of the second component would affect our quantitative results for the polar source by no more than 10%.

For both of these model components, we include an effective r_H-dependence power law of –2.6 over the observed range of heliocentric distances, based on the Cowan and A'Hearn (1979) vaporization model. The value is steeper than a canonical r_H^{-2}, because some of the solar radiation is used to heat, rather than vaporize, the ice. For the polar source, we also use the vaporization calculation for a sub-solar point, combined with the sine of the sub-solar latitude to account for the incident angle of the solar radiation. Because our solution for the pole orientation implies that the sub-solar latitude at +119 days (our last photometric data) should have been –17°, we assume that water was no longer being released by the polar source. Therefore, we attribute the measured water production, 1.0×10^{27} molecules s^{-1}, as coming entirely from the isotropic source. Using our adopted vaporization r_H-dependence, the isotropic component at perihelion would be 2.4× larger, i.e. 2.4×10^{27} molecules s^{-1}. Our best determined water production rate near perihelion occurs at approximately +5 days, which is closely bracketed by numerous observations from the 1988 and 2001 apparitions, with a total water production rate of 2.4×10^{28} molecules s^{-1}. From this, we can conclude that the polar source contributed 90% of the total water production at +5 days if the second component is isotropic, and as much as 100% if the second component is a southern hemisphere source which is turned off at perihelion. We will proceed using the former assumption.

Knowing the sub-solar latitude at +5 days was +51°, we can first compute what the polar source production rate would have been if the sun were directly overhead at perihelion. This value, 2.8×10^{28} molecules s^{-1}, can then be used to compute the water production from the polar source as a function of time throughout the apparition. Combining both components, we obtain the total water production, shown as the dotted curve in the bottom panel of Figure 10. Clearly evident is a very sharp drop in the production rate near ΔT = +80 day as the sub-solar latitude approaches the equator. However, this abrupt drop is somewhat artificial because the model thus far has treated the polar source region as a point source. In reality, the region must subtend an area at least as large as required to produce the measured water production. Again using Cowan and A'Hearn's vaporization model for a sub-solar point calculation, coupled with the measured values, we obtain a value for the required polar source area of about 3.5 km^2.

By comparing this area with an approximate total surface area of the nucleus, we can derive a fractional active area and a source radius in degrees. For the nucleus area, we assume nucleus dimensions of 4 × 4 × 8 km based on the HST and DS1 measurements; although Lamy *et al.* (1998) found dimensions of 8.8±0.6 by 3.6±0.3 km based on their lightcurve and assuming a 4% albedo and prolate spheroid shape, Soderblom *et al.* (2002) give a value for the long axis of 8 km. A prolate spheroid 8×4×4 km in size corresponds to an area

of 86 km^2, resulting in a fractional active area for the polar source of 4.1%. Assuming a spherical approximation for the nucleus, this fractional area corresponds to a equivalent source radius of about 23°.

Using this source radius, we adjusted our Monte Carlo jet model accordingly, yielding the illumination efficiency at locations within the source region as a function of time, and the results could be substituted for the original point source solution. Not surprisingly, the resulting water production curve matched the original point source model throughout the orbit except when the sub-solar latitude was near the equator. However, in this brief interval, the rate of water release was always larger from the broad source model as compared to the point source model. This is because the portion of the source region nearest to the subsolar point dominates the production at extreme sun angles. The resulting water production is shown in Figure 10 as the dashed curve, and this result converges with the point source solution at approximately +120 days, when only a very small portion of the 23° radius source is obliquely illuminated by the sun. As seen in Figure 12, this model solution, tied to measured water production rates at only two values of ΔT (+5 and +119 day), is an excellent fit to the measured water production throughout the apparition. Therefore, we conclude that Borrelly's exceptionally steep r_H-dependence of water following perihelion is caused by a simple, but extreme, change in solar illumination of a source region located at the pole.

Total Water Production

By integrating our model water production rate throughout an apparition, we can closely estimate the total amount of water sublimated each orbit. Based on an interval of –240 to +240 days, slightly greater than plotted in the bottom panel of Figure 10, we obtain a value of 3.6×10^{35} water molecules, corresponding to 1.1×10^{10} kg. From the trends in production rates at either end of this time span, coupled with the computed sub-solar latitude, we estimate that no more than an additional few percent of water is released outside of this interval during the remaining 5.6 years of an orbital period. Assuming that the polar source region contributes about 90% of the total water release, we require that 1.0×10^{10} kg of water be vaporized from an effective source area of 3.5 km^2. For a density of 1.0 gm cm^{-3}, this corresponds to a depth of about 2.9 m, while densities of 0.5 and 0.3 gm cm^{-3} would correspond to depths of about 5.8 and 9.7 m, respectively. Note that Farnham and Cochran (2002) compute a bulk density for Borrelly of 0.49 gm cm^{-3} and a range of between 0.29 and 0.83 gm cm^{-3}, based on their pole solution and source location, coupled with our water production curve and published non-gravitational acceleration terms. If this rate of depletion was maintained over the past century, this implies a total of 50-130 m of ice, a large but not unreasonable amount given Borrelly's minor axis diameter of 4 km.

Dust Behavior

We have already noted that the peak water production occurred approximately 3 weeks prior to perihelion. Using cumulative water production values from our model, we also find that one-half of the total water vaporization takes place between approximately -80 and +6 days, with the other half divided equally before and after these ΔTs. The mid-point in total water release occurs approximately 5 weeks before perihelion, or 2 weeks before peak production. From these results, we believe we can provide a qualitative explanation for several aspects of our dust observations. First, the $A(\theta)f\rho$ values for the dust were shown to have almost no

asymmetry surrounding perihelion, and the post-perihelion r_H-dependence was much shallower than for the gas species, with $A(\theta)f\rho$ decreasing by only 3× when the gas production rate decreased by 20-25×. Because dust grains are only dragged off of the surface of the nucleus by the gas flow, one would expect that the *actual* dust production rate would also decrease by an amount similar to the water production rate. This simple view, however, is based on the standard assumption that the physical nature of the dust grains remains constant throughout the apparition, i.e. the same particle size distribution and outflow velocities. In principle, an increasing rate of fragmenting grains late in the apparition could explain the relatively small r_H–dependence in measured $A(\theta)f\rho$ values, but this would require a change in the physical properties of the dust grains. As we discuss next, we prefer a scenario in which the dust coma late in the apparition was dominated by large, slow-moving grains released much earlier in the apparition, at or near peak water production. It would be the continued presence of these large, old grains which would produce the relatively shallow r_H -dependence in the observed $A(\theta)f\rho$ values. Here, too, the properties of the observed dust grains would have changed substantially with time. In fact, we know of no scenario to explain the shallow r_H–dependence which does not involve either a significant change in grain properties or a substantial population of old grains. From this it is clear that the measured $A(\theta)f\rho$ values late in the apparition cannot correctly reflect the ongoing rate of release of dust grains as compared to earlier in the apparition.

We prefer our scenario of large, slow-moving grains to alternative scenarios for several reasons. Sufficiently heavy grains would have very low outflow velocities and only be very slowly affected by radiation pressure, thereby remaining in the coma for weeks or months following their release. Usually, micron-sized grains are the dominate source of reflected light observed in the visible portion of the spectrum and, because of their relatively high velocity and low mass, micron-sized grains only remain in the inner coma for a few days, at most. However, as Borrelly's primary source region shuts off as winter rapidly arrives (see Figure 10), the release of dust grains would cease and progressively only more massive and slower-moving grains would remain in the inner coma. An alternative is to invoke icy grains in some manner to explain the shallow r_H–dependence, such as the cause of fragmenting grains or as a source of water production. However, it is difficult to imagine icy grains lasting weeks or months inside of 2 AU from the Sun. And if icy grains supplied a significant source of the observed water production, then the decrease in water production from the surface of the nucleus would have to be even steeper than we measured, only compounding the problem of the difference in water and dust r_H–dependencies.

Our preferred scenario is supported by several measured characteristics of the dust jet. We mentioned in Section V that the distance of the peak brightness along the jet progressively moved outward during the months following perihelion. From our pole solution, we compute the sub-Earth latitude (see Table VI) and, knowing the jet is aligned along the rotation axis, compute the projection effect for the jet as a function of time. Combining our earlier measurements of the projected distance of the peak in brightness along the jet, we compute deprojected distances for this peak brightness in November and December as $\sim 3.7\times10^4$ and $\sim 4.4\times10^4$ km, respectively, as compared to $<10^4$ km in September. Note that this change in distance is consistent with an assumption that the bulk of the larger-sized grains were released near the peak water production, i.e. –20 days. From these positional measurements, we obtain a very approximate outflow velocity for these large grains of about 5 m s^{-1}. Moreover, following the expected shutdown of the source region in December, the remnant of the dust jet was visible in 2002 January, February, and March by

ourselves and by Farnham and Cochran (2002). This feature, which is detached from the nucleus region, has a curvature and location, ~4.9×10^4 km in January, consistent with old, very slowly moving grains which are only beginning to be significantly affected by radiation pressure.

A significant population of large, slow moving grains can also explain the trends we previously detected for dust colors as a function of distance from the nucleus near perihelion, and the change in dust radial profiles as a function of time. Near perihelion, we showed in Section IV that the dust color was redder within apertures having projected radii of less than about 2×10^4 km than for larger radii, while in Section V we noted that the peak brightness along the jet was somewhat less than 1×10^4 km. Since larger grains are expected to exhibit significant reddening as compared to smaller dust grains, we attribute the reddening in smaller apertures to the large, slow moving grains. The change in the radial profiles as a function of distance from the nucleus and time from perihelion shown in Figures 3 and 4 are also completely consistent with the motion of the large grains in the jet through the apparition. Note that this scenario does not require two separate grain populations. Rather, we hypothesize a particle size distribution whose threshold size for entrainment in the outflowing gas varies with the water production rate. While the widest range of particle sizes would be released near perihelion, the maximum grain size lifted off of the surface would be expected to decrease as the water production drops, with only relatively small particles still being released just prior to the source shutting down. This may explain why modeling of Hanner *et al.*'s (1996) mid-IR spectra by Li and Greenberg (1998) resulted in the determination of grain properties which were apparently more processed, less fluffy, and more small grains than observed in 1P/Halley — the Borrelly spectra were obtained in a very small aperture centered on the nucleus 6 weeks following perihelion, a time and location consistent with the production of small grains.

As the source shuts-off, the smaller grains are rapidly removed from the coma by radiation pressure, leaving the largest grains behind. Therefore, while large grains do not usually contribute a significant amount of light in the visible spectrum because their contribution is overwhelmed by the more efficiently scattering small grains, in this instance the large grains become progressively more important as the source shuts-off. Moreover, this scenario directly implies that the high dust-to-gas ratio measured late in each apparition is an artifact of these large, old grains, and that the measured dust-to-gas ratio near perihelion is much more representative of Borrelly's actual composition. Although beyond the scope of this paper, a Finson-Probstein approach to modeling the evolution of the jet remnant, along with modeling of the westward extension of the secondary jet during 2002, could test our preferred scenarios for each feature and provide a quantitative determination of the range in grain sizes and other properties required to produce these unusual features.

VII. DEEP SPACE 1 ENCOUNTER

Thus far, we have largely neglected the encounter observations obtained from Deep Space 1 simply because our results and conclusions were independent of the DS1 results. However, there are several possible areas of comparison that can be made, and we can also interpolate some of our data to obtain our best estimates of the larger scale coma conditions at the time of the DS1 encounter.

One of the most significant measured quantity we can supply is our best estimate for Borrelly's water production rate at the time of the encounter: 2.3×10^{28} molecules s^{-1}. Other measured gas production rates can be extracted from Figure 11. Because of the significant aperture effects on our measured values for $A(\theta)f\rho$, an extraction for the inner-most coma is not as well constrained, but a reasonable estimate would be about 400-500 cm at green wavelengths.

Deep Space 1 imaging results have recently been reported by Soderblom *et al*. (2002). These revealed an extremely low average geometric albedo of 0.03±0.005, with localized albedo or reflectivities ranging from 0.01 to 0.035, perhaps even darker than measured by Giotto for Halley's nucleus (Keller *et al*. 1986). This value for Borrelly's geometric albedo is consistent with those of other measured Jupiter-family (J-F) comets. For instance, Neujmin 1 and Arend-Rigaux were both measured to have geometric albedos <0.03 prior to the Halley fly-bys (cf. Campins *et al*. 1987; Millis *et al*. 1985; Millis *et al*. 1988), while several other J-F comets and asteroids in comet-like orbits have geometric albedos of between 0.02 and 0.04 (cf. Jewitt 1991; Fernández *et al*. 2001). The DS1 images also revealed a highly elongated nucleus with an axial ratio of at least 2-to-1, again consistent with numerous minimum axial ratios measured for Jupiter-family comets (cf. Jewitt 1991). Somewhat unexpected was the discovery of three small jets emanating from the apparent polar region at skewed angles; it is unclear if they are associated with the much brighter jet seen at larger distances from the nucleus in the DS1 imaging. Soderblom *et al*. designate the core of this bright feature as the alpha jet, and note that it has a width of only a few kilometers at its base, appears to remain stationary to within ±5° in position during the spacecraft's approach, and is at an angle of about 30° to the Sun. From these observations, they conclude that the jet is nearly aligned with the rotation axis and that the sub-solar latitude was at ~60° north. This estimate can be compared with our model solution of +49° for the sub-solar latitude at the time of the DS1 encounter. Soderblom *et al*. also find that the associated direction of the jet is at $\alpha = 218.^{\circ}5\pm3^{\circ}$ and $\delta = -12.^{\circ}5\pm3^{\circ}$, differing from our own solution by about 4° and 7°, respectively, or a net offset between the solutions of 8°. It is therefore clear that their α jet is the progenitor of the jet we and the other groundbased investigators observed on far larger spatial scales. Indeed, the DS1 images also reveal a variety of interesting topography on the surface of the nucleus. Unfortunately, while individual components of a much weaker jet, designated as β by the DS1 investigators, can be traced back to darker, possibly depressed surface features (cf. Soderblom *et al*.), the α jet has not been successfully traced back to a particular topographic or albedo feature. From our estimate for the water vaporization rate from the polar jet's source region of 3-6 m per apparition, some evidence for long-term excavation would be expected. One might speculate that a slow migration of the source could occur as the vaporization process preferentially erodes one side of the source due to changing solar illuminations from long-term precession. Eventually, this process may cause the observed narrow "waist" of Borrelly's nucleus. A variety of other evolution scenarios for source regions and for a nucleus' rotation are presented by Sekanina (1991) and Samarasinha (2002), respectively.

VIII. DISCUSSION AND SUMMARY

Although Comet Borrelly is the third Jupiter-family comet visited by a spacecraft, it is the first to be imaged from up close, because the ICE spacecraft had no camera for its encounter with P/Giacobini-Zinner and Giotto's camera was disabled following closest approach during the Halley fly-by and therefore non-

operational at its subsequent encounter with P/Grigg-Skjellerup. While these new DS1 images have confirmed the current, general perception of the physical properties of comet nuclei, based primarily on the spacecraft encounters with Comet 1P/Halley in 1986, they have also shown that Borrelly's properties are more extreme than Halley's in many respects. Borrelly is more elongated and apparently has localized regions of even lower reflectivity than Halley. Its active source region covers a much smaller fraction of the surface of the nucleus and, being located at the pole, experiences extreme seasonal effects. While Halley and Borrelly presumably have different origins, with Halley coming from the Oort Cloud and Borrelly likely originating from the Kuiper Belt, none of these differing physical characteristics appear to be associated with these comets' origins. Rather, it seems much more likely that the differences between these two objects reflect different stages in physical evolution, with Borrelly being more evolved. One can easily imagine that within a few thousand years, if not within hundreds of years, the polar source region will either exhaust its supply of volatiles or be crusted over, similar to the remaining 96% of the surface. Once Borrelly becomes extinct, it might be quite difficult to distinguish it from other near-Earth asteroids (NEAs).

In many respects, Comet Borrelly is very representative of Jupiter-family (J-F) comets as a class. Like about 2/3rds of the J-F comets in the A'Hearn *et al*. (1995) database, it exhibits a strong asymmetry about perihelion in gas production rates. For a variety of reasons, A'Hearn *et al*. attributed these asymmetries to seasonal effects, rather than to thermal lags or exhaustion of source regions. We believe we have now, at least in the case of Borrelly, conclusively demonstrated for the first time this to be true. We have successfully modeled the jet orientation over the 1994 and 2001 apparitions, obtaining a tightly constrained pole orientation having an obliquity of 102.°7±0.°5 and an orbital longitude of the pole of 146±1°. Based on this solution, we have conclusively shown that a source region at or very near the rotation pole produces approximately 90% or more of the outgassing near perihelion, and we have demonstrated that peak solar illumination occurs several weeks before perihelion, in excellent agreement with our measured gas production rates. The fact that Borrelly exhibits the steepest r_H-dependence for water of any comet in our database is explained by the location of the source region, i.e. at the pole, coupled with the change of sub-solar latitude through the apparition, with the polar source no longer receiving any solar radiation only 4 months following perihelion. Other comets, presumably having either multiple source regions or sources located away from the pole, would be expected to show less extreme seasonal effects, which they do.

Borrelly is depleted in carbon-chain molecules, as are approximately one-half of all Jupiter-family comets in the A'Hearn *et al*. (1995) database. Borrelly's measured average dust-to-gas ratio is in the mid-range of all comets, but varies strongly following perihelion because the dust shows a much shallower r_H-dependence than any of the gas species. This behavior requires a significant change in the bulk properties of the dust during the apparition. We have shown that this behavior of the dust can be explained by a population of large, slow-moving grains released during peak water production in the weeks prior to perihelion. These old, large grains provide an ever-increasing proportion of the light measured at continuum wavelengths following perihelion simply because the source region progressively shuts down due to the drop in available solar radiation. As the source turns off, the supply of smaller grains diminishes while small grains already in the coma rapidly disperse due to radiation pressure effects. Although the large grains are not usually detected in the visible because they are overwhelmed by the more efficiently scattering small grains, once the smaller grains are gone, the remaining large grains are responsible for the light we see. The presence of

large grains is also consistent with the observed red color of the grains. Therefore, while the steep r_H-dependencies exhibited by the gas species reflect the near-instantaneous gas production, because of the gas' relatively high outflow velocities and relatively short lifetimes, the measured $A(\theta)f\rho$ values late in the apparition are dominated by old material, and do not reflect the ongoing rate of release of dust grains from the surface. This scenario of an appreciable population of old, slow moving grains is supported by observed aperture effects and the evolving appearance of the polar jet throughout the apparition.

Unfortunately, Comet Borrelly will be on the opposite side of the Sun from the Earth during each of the next two apparitions in 2008 and 2015, yielding very poor viewing geometries. The next reasonable opportunity to investigate the turn-on of the polar jet will have to wait until 2014, approximately 10 months before perihelion in 2015. Fortunately, many other comets have been measured to have either steep or strongly asymmetric r_H-dependencies, such as 49P/Arend-Rigaux, 67P/Churyumov-Gerasimenko, 21P/Giacobini-Zinner, 22P/Kopff, and 10P/Tempel 2 (cf. A'Hearn *et al*. 1995), and some of these will be well-placed during this decade to permit similar synergistic investigations.

ACKNOWLEDGEMENTS

We gratefully acknowledge the assistance of M. A'Hearn, L. French, D. Thompson, S. Sackey, P. Birch, E. Turtle, and R. Greer in the acquisition of some of the reported observations. We thank T. Farnham, A. Cochran, and N. Samarasinha for making available their results prior to publication and for numerous discussions which helped our overall understanding of Comet Borrelly's behavior. This work was funded by NASA Grants NAG5-7947 and NAG5-9009.

REFERENCES

A'Hearn, M. F., and R. L. Millis 1980. Abundance correlations among comets. *Astron. J.* **85**, 1528-1537.

A'Hearn, M. F., R. L. Millis, and P. V. Birch 1979. Gas and dust in some recent periodic comets. *Astron. J.* **84**, 570-579.

A'Hearn, M. F., R. L. Millis, D. G. Schleicher, D. J. Osip, and P. V. Birch 1995. The ensemble properties of comets: Results from narrowband photometry of 85 comets. *Icarus* **118**, 223-270.

A'Hearn, M. F., D. G. Schleicher, P. D. Feldman, R. L. Millis, and D. T. Thompson 1984. Comet Bowell 1980b. *Astron. J.* **89**, 579-591.

A'Hearn, M. F., H. Campins, D. G. Schleicher, and R. L. Millis 1989. The nucleus of Comet P/Tempel 2. *Astrophys. J.* **347**, 1155-1166.

Baum, W. A., T. J. Kreidl, and D. G. Schleicher 1992. Cometary grains. *Astron. J.* 104, 1216-1225.

Bockelée-Morvan, D., N. Biver, P. Colom, J. Crovisier, E. Gérard, L. Jorda, J. K. Davies, B. Dent, F. Colas, D. Despois, G. Paubert, and P. Lamy 1995. Visible and radio observations of Comet 19P/Borrelly. *Bull. Am. Astron. Soc.* **27**, 1144.

Boehnhardt, H., H. Drechsel, V. Vanysek, and L. Waha 1989. Photometric investication of comets Bradfield 1987S and P/Borrelly. *Astron. Astrophys.* **220**, 286-292.

Campins, H., M. F. A'Hearn, and L.-A. McFadden 1987. The bare nucleus of Comet Neujmin 1. *Astrophys.J.* **316**, 847-857.

Chofardet, P. 1913. Observations de comètes. *Bull. Astron.* **30**, 554-559.

Cochran, A. L., and E. S. Barker 1999. McDonald Observatory spectral observations of Comet 19P/Borrelly. *Icarus* **141**, 307-315.

Cochran, A. L., and D. G. Schleicher 1993. Observational constraints on the lifetime of cometary H2O. *Icarus* **105**, 235-253.

Cowan, J. J. and M. F. A'Hearn 1979. Vaporization of cometary nuclei: Light curves and lifetimes. *Moon and Planets* **21**, 155-171.

Farnham, T. L., and A. L. Cochran 2002. A McDonald Observatory study of Comet 19P/Borrelly: Placing the Deep Space 1 observations into a broader context. *Icarus*, in press.

Farnham, T. L., D. G. Schleicher, and M. F. A'Hearn 2000. The HB narrowband comet filters: Standard stars and calibrations. *Icarus* **147**, 180-204.

Farnham, T. L., D. G. Schleicher, W. R. Williams, B. R. Smith 1999. The rotation state and active regions of Comet Hale-Bopp (1995 O1). *Bull. Am. Astron. Soc.* **31**, 1120.

Fernández, Y. R., D. C. Jewitt, and S. S. Sheppard 2001. Low albedos among extinct comet candidates. *Astrophys.J.* **553**, L197-L200..

Fulle, M. A. Milani, and L. Pansecchi 1997. Tomography of a sunward structure in the dust tail of comet 19P/Borrelly. *Astron. Astrophys.* **321**, 338-342.

Gustafson, B., and L. Kolokolova 1999. A systematic study of light scattering by aggregate particles using the microwave analog technique: Angular and wavelength dependence of intensity and polarization. *J. Geophysical Research* **104**, 31711-31720.

Hanner, M. S., D. K. Lynch, R. W. Russell, J. A. Hackwell, R. Kellogg, D. Blaney 1996. Mid-infrared spectra of Comets P/Borrelly, P/Faye, and P/Schaumasse. *Icarus* **124**, 344-351.

Hanner, M. S., and R. L. Newburn 1989. Infrared photometry of comet Wilson (1986l) at two epochs. *Astron. J.* **97**, 254-261.

Jeffers, H. M. 1926. Measures of comets. *Lick Obs. Bull.* **12**, 124-129.

Jewitt, D. 1991. Cometary photometry. In *Comets in the Post-Halley Era. Vol. 1* (R. L. Newburn, Jr., M. Neugebauer, and J. Rahe, Eds.) pp. 19-65. Kluwer Academic Publishers, Dordrecht, The Netherlands.

Jewitt, D., and K. J. Meech 1986. Cometary grain scattering versus wavelength, or, "What color is comet dust?" *Astrophys. J.* **310**, 937-952.

Keller, H. U., C. Arpigny, C. Barbieri, R. M. Bonnet, S. Cazes, M. Coradini, C. B. Cosmovici, W. A. Delamere, W. F. Huebner, D. W. Hughes, C. Jamar, D. Malaise, H J. Reitsema, H. U. Schmidt, W. K. H. Schmidt, P. Seige, F. L. Whipple, and K. Wilhelm 1986. First Halley Multicolour Camera imaging results from Giotto. *Nature* **321**, 320-326.

Keller, H. U., R. Kramm, N. Thomas 1988. Surface features on the nucleus of Comet Halley. *Nature* **331**, 227-231.

Lamy, P. L., I. Toth, and H. A. Weaver 1998. Hubble Space Telescope observations of the nucleus and inner coma of comet 19P/1904 Y2 (Borrelly). *Astron. Astrophys.* **337**, 945-954.

Li, A., and J. M. Greenberg 1998. The dust properties of a short period comet: comet P/Borrelly. *Astron. Astrophys.* **338**, 364-370.

Meredith, N. P., M. K. Wallis, and D. Rees 1989. The anomalous behaviour of C_2 in P/Borrelly 1987p. *MNRAS* **240**, 647-655.

Millis, R. L., M. F. A'Hearn, and H. Campins 1985. The nucleus and coma of Comet P/Arend-Rigaux. *Bull. Am. Astron. Soc.* **17**, 688.

Millis, R. L., M. F. A'Hearn, and H. Campins 1988. An investigation of the nucleus and coma of Comet P/Arend-Rigaux. *Astrophys.J.* **324**, 1194-1209.

Mueller, B. E. A., and N. H. Samarasinha 2002. Visible lightcurve observations of comet 19P/Borrelly. Submitted to *Earth Moon Planets*.

Newburn, R. L., and H. Spinrad 1984. Spectrophotometry of 17 comets. I. The emission features. *Astron. J.* **89**, 289-309.

Samarasinha, N. H. 2002. Cometary spin states, their evolution, and the implications. In *Proceedings of the IAU Colloquium 168, "Cometary Nuclei in Space and Time,"* in press.

Samarasinha, N. H., and B. E. A. Mueller 2002. Spin axis direction of comet 19P/Borrelly based on observations from 2000 and 2001. Submitted to *Earth Moon Planets.*

Schleicher, D. 2001. Photometry of Comet 19P/Borrelly. *IAU Circ.* 7722.

Schleicher, D. G., R. L. Millis, and P. V. Birch 1998b. Narrowband photometry of Comet P/Halley: Variation with heliocentric distance, season, and solar phase angle. *Icarus* **132**, 397-417.

Schleicher, D. G., and L. M. Woodney 2002. Analyses of dust coma morphology of Comet Hyakutake (1996 B2) near perigee: Outburst behavior, jet motion, source region locations, and nucleus pole orientation. Submitted to *Icarus*.

Schleicher, D. G., T. L. Farnham, B. R. Smith, E. A. Blount, E. Nielsen, S. M. Lederer 1998a. Nucleus properties of Comet Hale-Bopp (1995 O1) based on narrowband imaging. *Bull. Am. Astron. Soc.* **30**, 1063-1064.

Schleicher, D. G., and D. J. Osip 2002. Long and short-term photometric behavior of Comet Hyakutake (1996 B2). *Icarus*, in press.

Sekanina, Z. 1979. Fan-shaped coma, orientation of rotation axis, and surface structure of a cometary nucleus. I. Test of a model on four comets. *Icarus* **37**, 420-442.

Sekanina, Z. 1991. Cometary activity, discrete outgassing areas, and dust-jet formation.. In *Comets in the Post-Halley Era. Vol. 2* (R. L. Newburn, Jr., M. Neugebauer, and J. Rahe, Eds.) pp. 769-823. Kluwer Academic Publishers, Dordrecht, The Netherlands.

Scheeres, D. J., S. J. Ostro, R. A. Werner, E. Asphaug, and R. S. Hudson 2000. Effects of Gravitational Interactions on Asteroid Spin States. *Icarus* **147**, 106-118.

Soderblom, L. A., D. C. Boice, D. T. Britt, R. H. Brown, B. J. Buratti, M. D. Hicks, R. M. Nelson, J. Oberst, B. R. Sandel, S. A. Stern, N. Thomas, R. V. Yelle 2001. Observations of Comet 19P/Borrelly from the Miniature Integrated Camera and Spectrometer (MICAS) aboard Deep Space 1 (DS1). *Bull. Am. Astron. Soc.* **33**, 1087.

Soderblom, L. A., T. L. Becker, G. Bennett, D. C. Boice, D. T. Britt, R. H. Brown, B. J. Buratti, C. Isbell, B. Giese, T. Hare, M. D. Hicks, E. Howington-Kraus, R. L. Kirk, M. Lee, R. M. Nelson, J. Oberst, T. C. Owen, M. D. Rayman, B. R. Sandel, S. A. Stern, N. Thomas, R. V. Yelle 2002. Observations of Comet 19P/Borrelly by the Miniature Integrated Camera and Spectrometer aboard Deep Space 1. *Science*, **296**, 1087-1091.

van Biesbroeck, G. 1914. Observations faites a l'équatorial de 38 centimètres d'ouverture de 1907 a 1912. *Ann. Obs. Roy. Belg.* **13**, 339-618.

van Biesbroeck, G. 1920. Observations of comets. *Astron. J.* **32**, 89-93.

van Biesbroeck, G. 1927. Observations of comets at the Yerkes Observatory. *Astron. J.* **37**, 61-68.
van Biesbroeck, G. 1934. Observations of comets at Yerkes Observatory. *Astron. J.* **43**, 17-24.
Williams, I. P., P. J. Andrews, A. Fitzsimmons, and G. P. Williams 1990. The ratio of production rates of C_2 and C_3 to CN in six comets. In *Asteroids, Comets, Meteors, III* (C.-I. Lagerkvist, H. Rickman, P. A. Lindblad, and M. Lindgren, Eds.), pp. 471-474. Reprocentralen HSC Uppsala, Sweden.
Yeomans, D. K. 1972. A non-Newtonian orbit for Periodic Comet Borrelly. In The Motion, Evolution of Orbits, and Origin of Comets (G. A. Chebotarev, E. I. Kazimirchak-Polonskaya, and B. G. Marsden, Eds.), pp. 187-189. D. Reidel Publishing Co., Dordrecht, Holland.

FIGURE CAPTIONS

Figure 1. Representative red continuum (left) and CN (right) images from 2001 September 22, obtained only 12 hours before the DS1 encounter. The top panels are unenhanced, except for a logarithmic stretch, while the bottom panels have been enhanced by dividing by the azimuthal median of each image. The CN frame was continuum subtracted, so the resulting image is essentially only CN gas emission. As displayed, these trimmed images are 194,000 km on a side, with north at the top and east to the left. The position angle of the sun is 101°. Note the relatively narrow sunward dust jet as compared to the associated CN jet which is very broad in appearance, presumably due to CN's randomly distributed excess velocity during its creation from parent species such as HCN.

Figure 2. Log of the production rates for each observed molecular species and $A(\theta)f\rho$ for the green continuum plotted as a function of the log of the heliocentric distance. Different symbols distinguish the four apparitions (see key at top); filled symbols represent data obtained before perihelion while open symbols are used for post-perihelion measurements. Vertical dotted lines representative perihelion distance; the left-most position is for 1981 prior to Borrelly's orbit being perturbed. Dashed lines are linear least-squares fits only for the post-perihelion data, excluding the 1981 measurements, and all gas species show very steep r_H-dependences as compared to the dust.

Figure 3. Relative log $A(\theta)f\rho$ values as a function of the log of the projected aperture radii. Data obtained within a span of 3 days or less are indicated by similar shading; different observing runs are distinguished by alternating open and shaded symbols. Data sets are normalized in Δ log $A(\theta)f\rho$ to a common aperture size, but shifted vertically based on the time from perihelion (right-hand axis labels). Uncertainties are all smaller than the plotted data points. It is evident that the derived value of $A(\theta)f\rho$ nearly always decreases with increasing ρ, and the rate of decrease accelerates at large log ρ. The data also suggest that the slopes become less steep later in the apparition, or that the departure from a canonical $1/\rho$ radial profile (which would yield a constant value for $A(\theta)f\rho$) moves outward as a function of time. The solid curve plotted in the right-hand panel represents a series of extracted $A(\theta)f\rho$ values from narrowband imaging on 2001 September 22, only 12 hours prior to the DS1 encounter.

Figure 4. Radial profiles of the dust, shown as the log of the normalized flux as a function of the log of the projected distance from the nucleus. Extractions are for a 20° wedge centered on the sunward jet (when the jet is active; shown as a solid curve), a similar wedge centered in the anti-sunward direction, i.e. the tail

(dashed curve), and the average of two 90° wedges centered in the perpendicular direction to the sun-tail line (dot-dash curve). A canonical $1/\rho$ profile is overlaid as the dotted line. Note that the sunward jet is brighter than other directions until late in the apparition (time from perihelion in units of days are given above each date), and that the peak relative brightness along the jet as compared to the ambient coma moves slowly outward with time. By 2002 January 12, the jet's source has turned off, and only a remnant is visible at larger ρ from large, old, very slow-moving grains.

Figure 5. Log of the dust colors as a function of the log of r_H. Symbols are the same as in Figure 1. The color of the dust is shown as the differential $A(\theta)f\rho$ for blue and UV continuum bandpasses (top), green and blue (middle), and green and UV (bottom). Note that the dust colors do not show a trend with heliocentric distance. A portion of the scatter among data points in the bottom panel is due to changes in the spectral locations of the UV and green continuum bandpasses for the different filter sets.

Figure 6. Dust colors in as a function of aperture size. The color of the dust is shown as a reflectivity normalized to 5240 or 5260 Å for the UV and blue continuum bandpasses. Note the trend in reflectivity in the UV with aperture size for aperture radii larger than about 2×10^4 km. No such trend is evident at the blue continuum bandpass, but for a smaller range of aperture sizes.

Figure 7. Dust reflectivity as a function of wavelength. Reflectivities are normalized to either 5240 or 5260 Å. Different symbols distinguish the four apparitions (see key at top); differently sized symbols represent the average value within a range of aperture sizes (log ρ; see key at right). To improve S/N, only observations obtained at $r_H < 1.45$ AU were included in the averages. Crosses represent values extracted from 2001 September 22 narrowband images. Note the strong trend in reflectivity with aperture size in the near-UV. The dashed line is an unweighted fit to the intermediate-sized aperture extractions (ρ from 1×10^4 to 4×10^4 km); the CCD red continuum data confirm that the strong reddenning of the dust grains seen at shorter wavelengths continues into the very near-IR, unlike for some other comets.

Figure 8. Representative dust images, after enhancement using the azimuthal median technique. One image is shown from each observing run, except for 2001 September, when a pair of images bracketing either side of the DS1 encounter by 12 hr are shown. Each frame is 97,000 km on a side, with north at the top and east to the left. The projected direction of the Sun is indicated on each frame (red arrow), along with the measured position of the primary, sunward jet (orange arrow) when feasible. Note that the brightness of the jet as compared to the tail progressively decreases throughout an apparition. The peak brightness along the jet moves outward with time, consistent with a substantial population of large, very slow moving grains. By $\Delta T \geq +100$ day, the jet has essentially shut-off, and only a remnant feature is visible towards the south-southeast..

Figure 9. Representative polar coordinate θ-ρ images of the primary, sunward jet. Enhanced images, as shown in Figure 8, have been unwrapped, and resampled in 1° bins in the θ-direction, while the ρ direction has been binned to 4× the original pixel scale for each apparition. Note the slow, outward motion of the peak brightness in the jet during an apparition. Intensity profiles were created and used to measure the position

angle (θ) of the peak intensity and the half-power points at each binned distance for each frame. The average extracted values for each night are listed in Table VI.

Figure 10. Solar illumination as a function of time from perihelion based on our solution of the pole orientation in 2001. The sub-solar latitude (top) peaks at –43 days and reaches the equator at +82 days. The log of the water production rate (bottom) assumes the polar source region produces approximately 90% of the water at +5 days, with the remainder released isotropically from the entire surface, except as modified by available solar radiation (see text for additional justifications for our model parameters). The dotted curve is for a model assuming a point source at the pole, while the dashed curve assumes a polar source having a radius of 23°, consistent with the surface area required to vaporize water ice at the rate observed.

Figure 11. Log of the production rates for each observed molecular species and $A(\theta)f\rho$ for the green continuum plotted as a function of time from perihelion. The DS1 encounter (dashed vertical line) took place 8 days following perihelion. Symbols are the same as in Figure 1. A canonical water vaporization model is shown as a dotted curve, transposed for each species by scaling the near-perihelion measurements. The dashed curve represents our model solution for water vaporization originating primarily from the polar source region, again for each species. Note the good-to-excellent fit of the model solution to the various gas species, except in 1981 when the heliocentric distances are smaller for any given ΔT. In contrast, this curve does not fit the dust measurements. While some of the scatter in the dust data is due to aperture effects (see Figure 3), the dust generally has a much more shallow fall-off following perihelion.

Figure 12. Log of the water production rate as a function of the log of r_H. Symbols are the same as in Figure 1. Vectorial-equivalent water production rates are computed from the Haser OH production rates (see text for details). The water production r_H-dependence after perihelion is extremely steep compared to that expected from a basic water vaporization model (short-dashed curve). The predicted water production curve based on our preferred model solution is shown as the long-dashed curve. Here, the model is composed of a 23° radius source located at the pole combined with an isotropic component; the size of the polar source is constrained by vaporization model and the measured length of the nucleus. A preliminary model solution, assuming the polar source is point-sized, is shown as the dotted curve. Besides being physically unrealistic, this preliminary solution does not fit the observations near log $r_H = 2.3$.

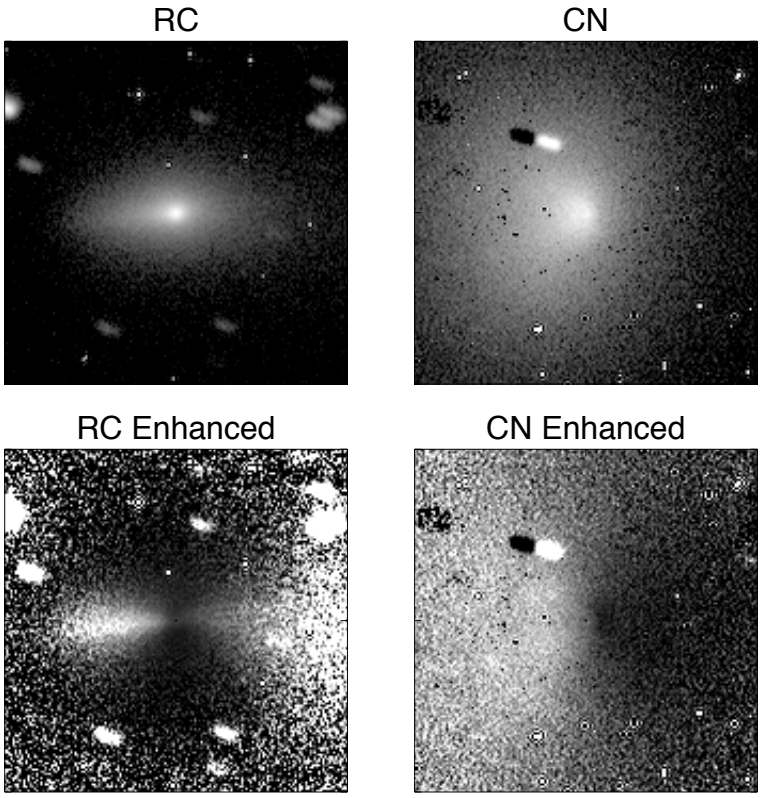

Figure 1

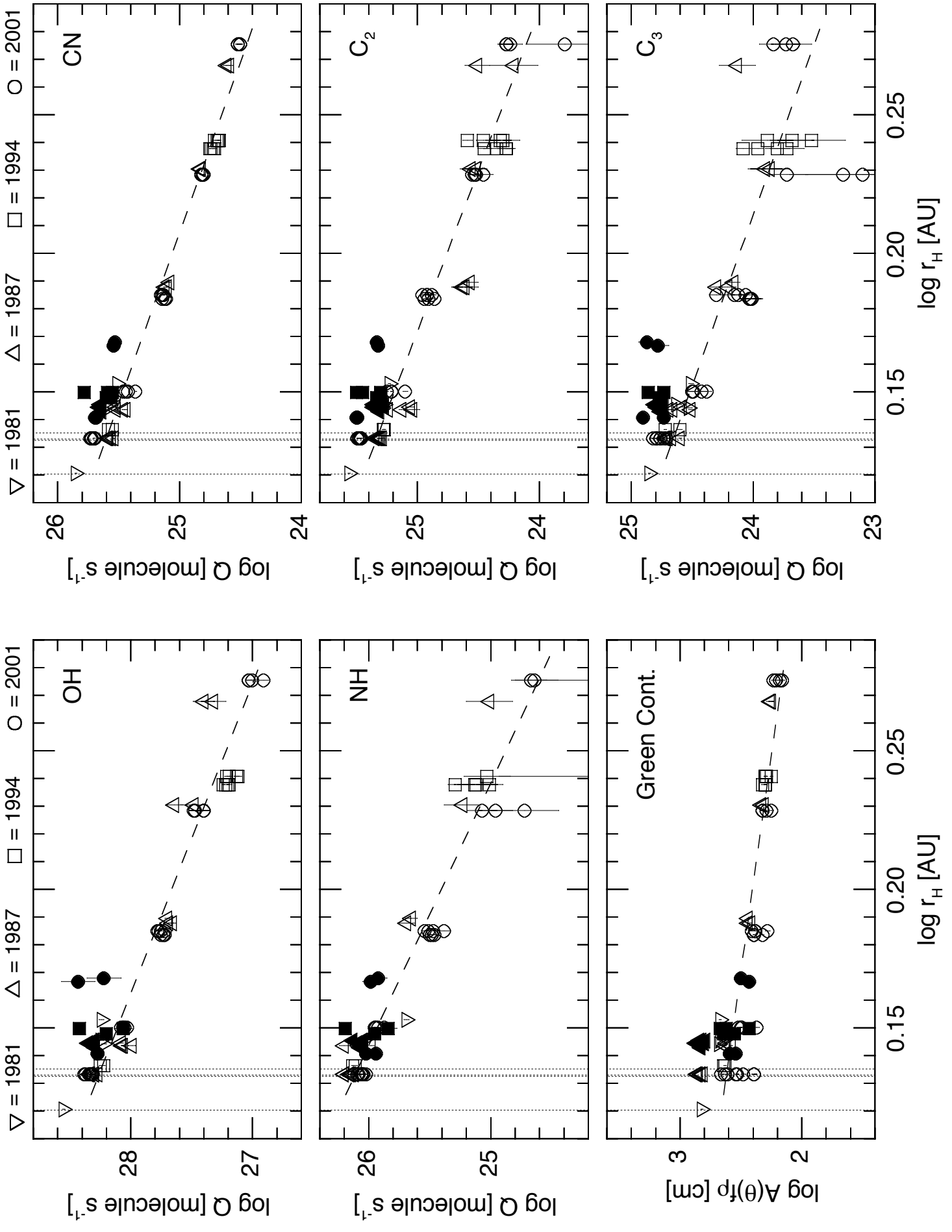
▽ = 1981
△ = 1987
□ = 1994
○ = 2001
CN
C2
C3
OH
NH
Green Cont.
log Q [molecule s-1]
log Af(θ)ρ [cm]
log rH [AU]

Figure 2

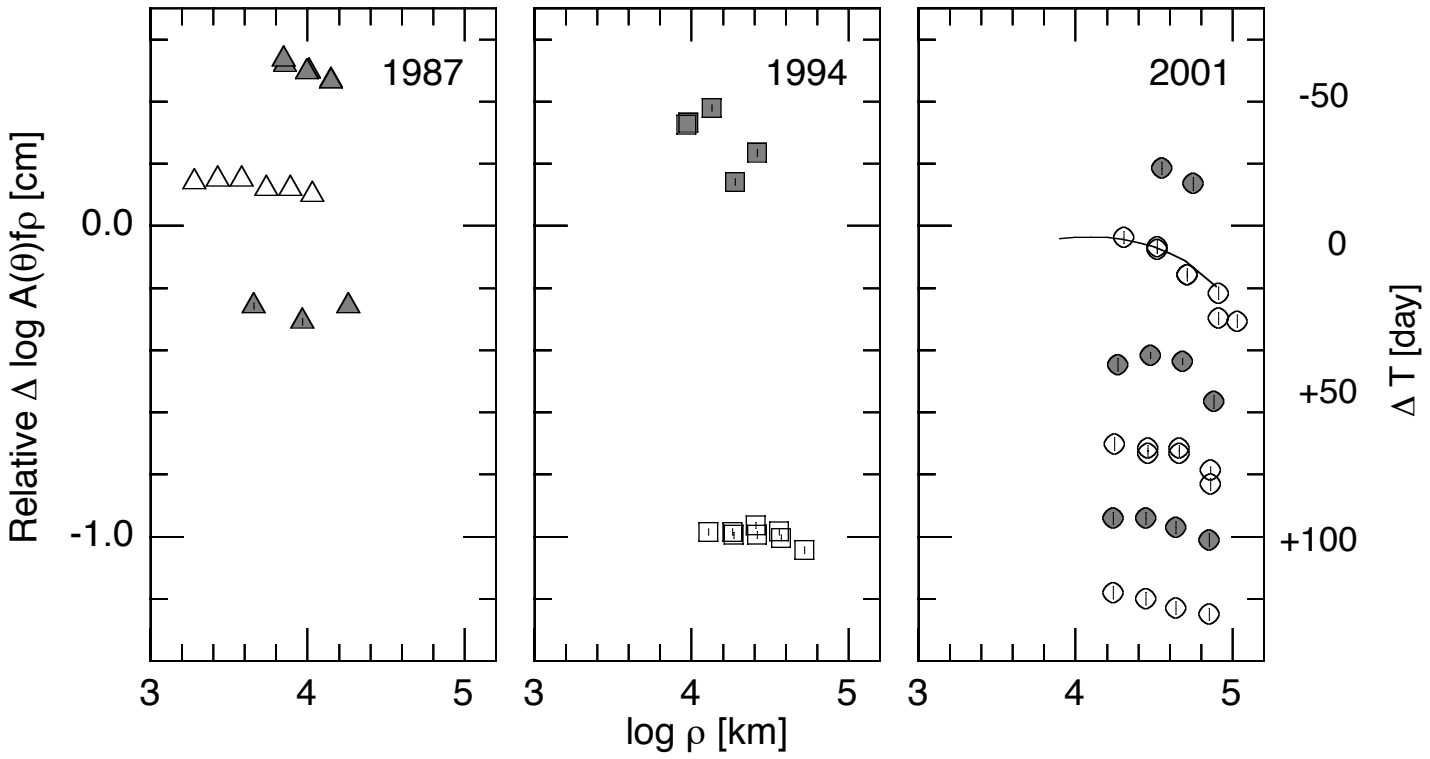
1987
1994
2001
Relative Δ log A(θ)fρ [cm]
0.0
-1.0
-50
0
+50
+100
Δ T [day]
3
4
5
log ρ [km]

Figure 3

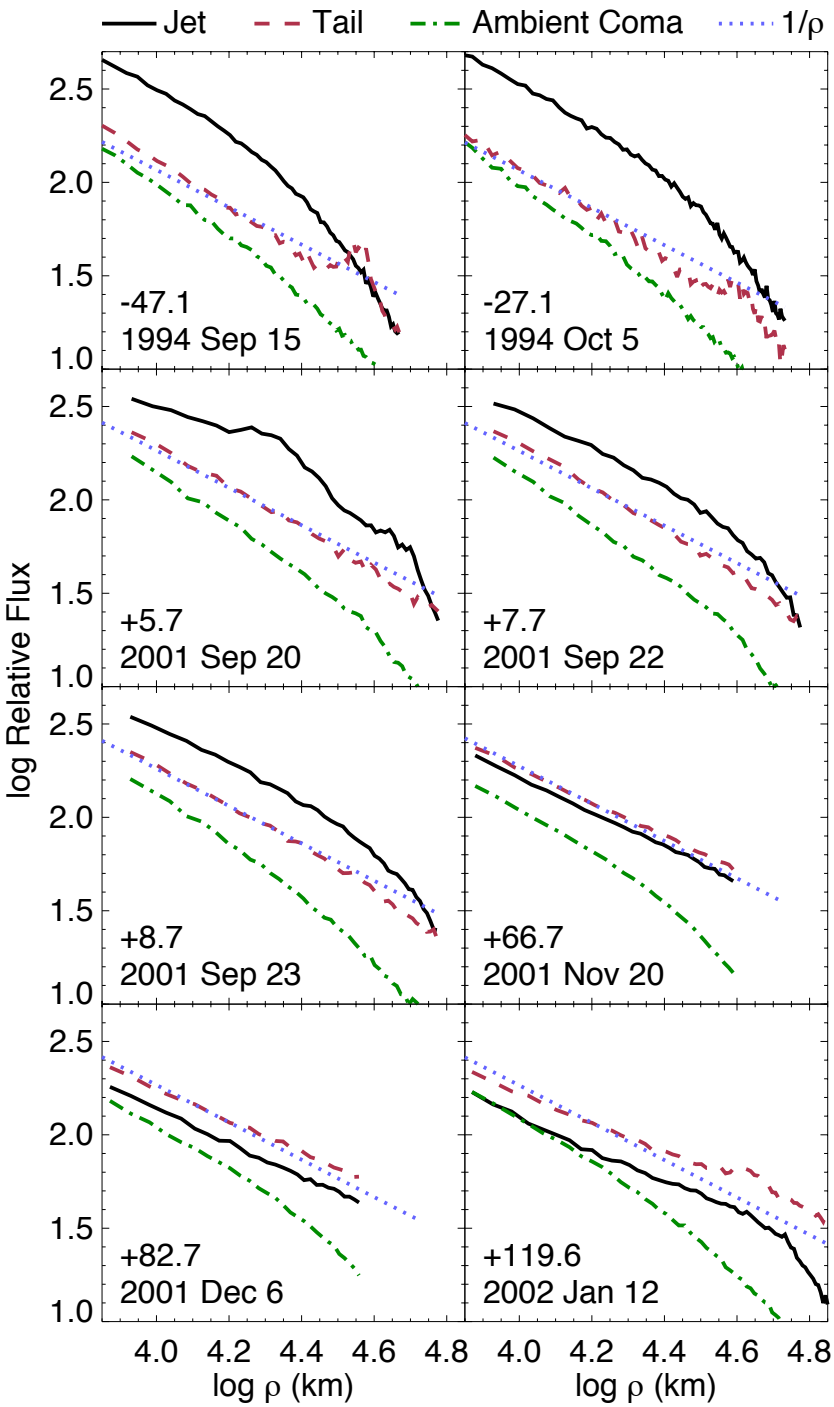
Jet
Tail
Ambient Coma
1/ρ
log Relative Flux
-47.1
1994 Sep 15
-27.1
1994 Oct 5
+5.7
2001 Sep 20
+7.7
2001 Sep 22
+8.7
2001 Sep 23
+66.7
2001 Nov 20
+82.7
2001 Dec 6
+119.6
2002 Jan 12
log ρ (km)
log ρ (km)

Figure 4

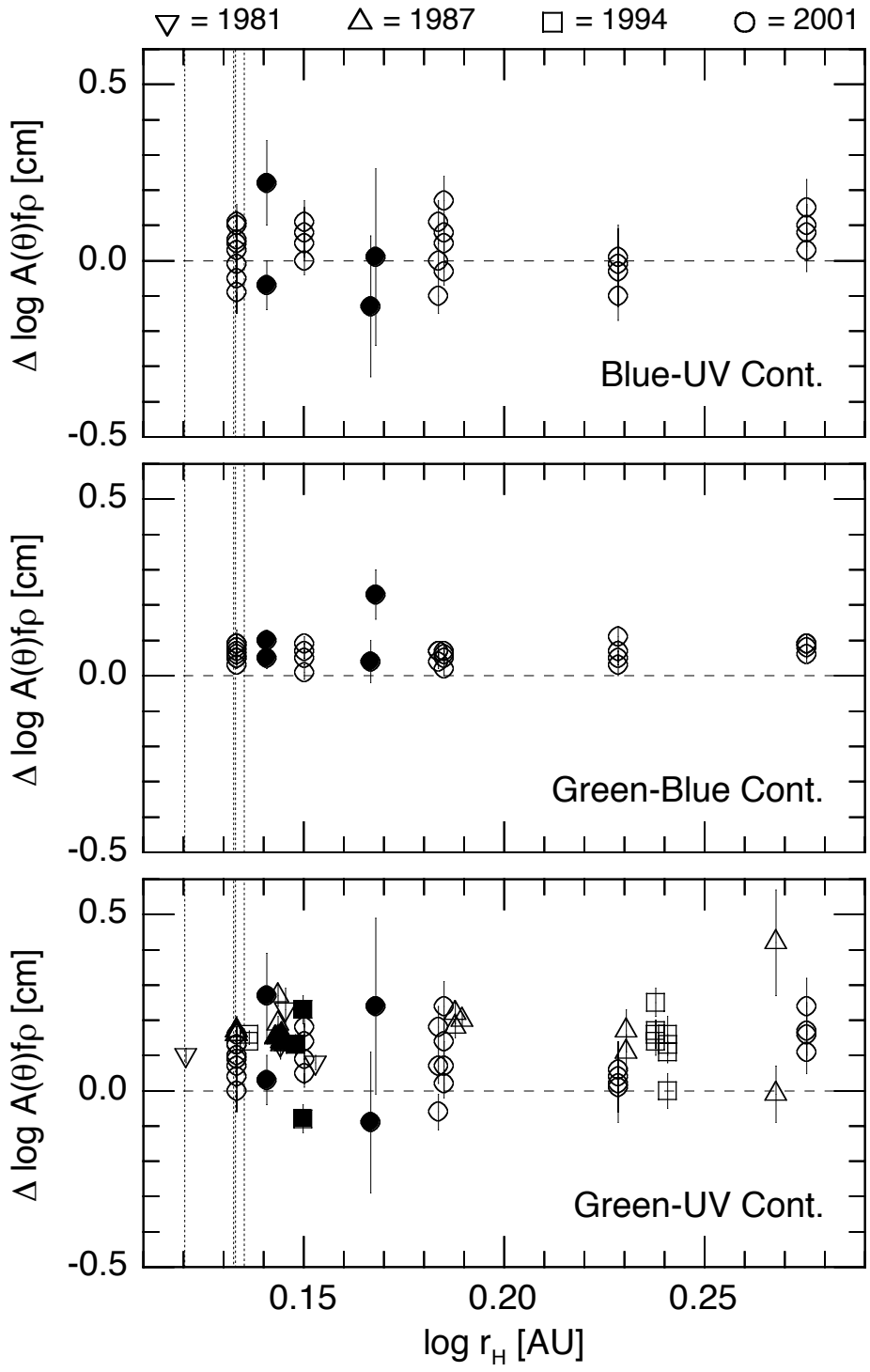
▽ = 1981
△ = 1987
□ = 1994
○ = 2001
Δ log A(θ)fρ [cm]
0.5
0.0
-0.5
Blue-UV Cont.
Green-Blue Cont.
Green-UV Cont.
0.15
0.20
0.25
log r_H [AU]

Figure 5

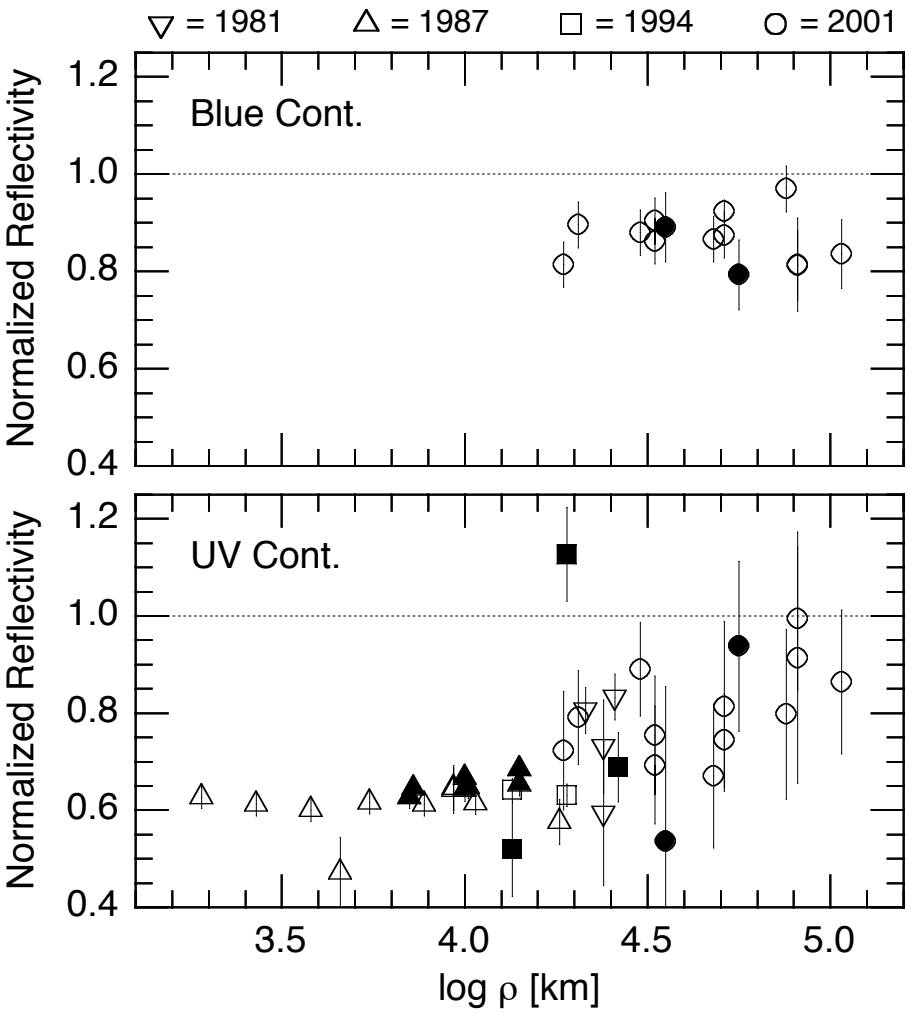
▽ = 1981
△ = 1987
□ = 1994
○ = 2001
Blue Cont.
UV Cont.
Normalized Reflectivity
1.2
1.0
0.8
0.6
0.4
3.5
4.0
4.5
5.0
log ρ [km]

Figure 6

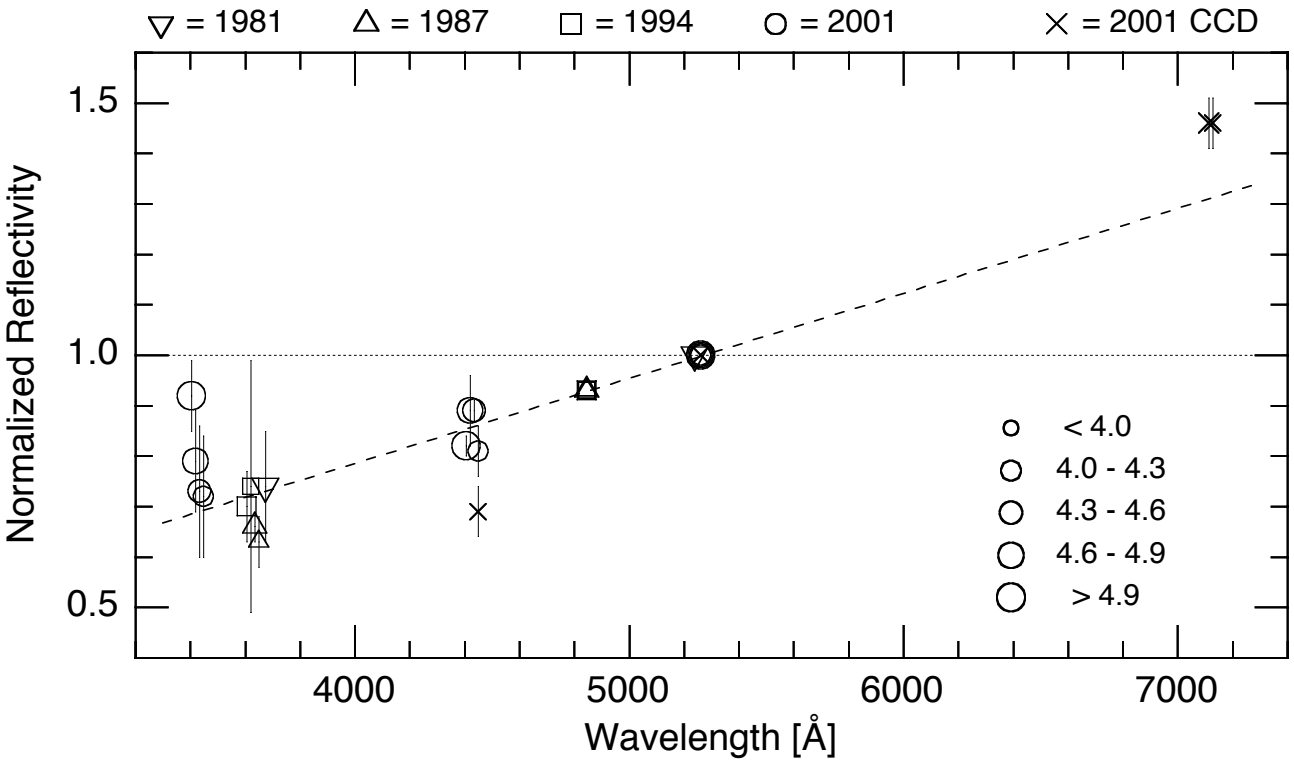
▽ = 1981
△ = 1987
□ = 1994
○ = 2001
× = 2001 CCD
Normalized Reflectivity
1.5
1.0
0.5
4000
5000
6000
7000
Wavelength [Å]
< 4.0
4.0 - 4.3
4.3 - 4.6
4.6 - 4.9
> 4.9

Figure 7

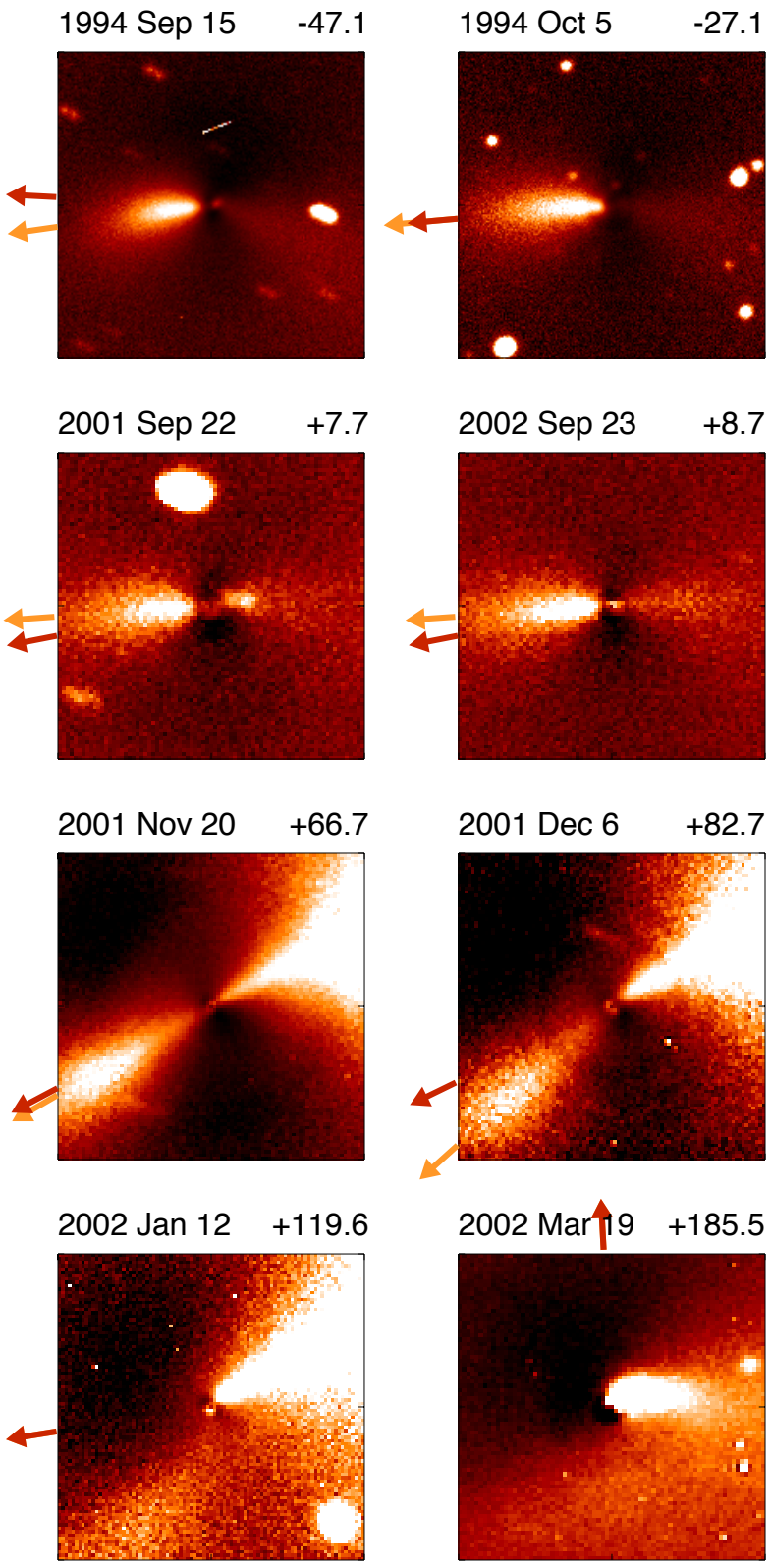
1994 Sep 15 -47.1
1994 Oct 5 -27.1
2001 Sep 22 +7.7
2002 Sep 23 +8.7
2001 Nov 20 +66.7
2001 Dec 6 +82.7
2002 Jan 12 +119.6
2002 Mar 19 +185.5

Figure 8

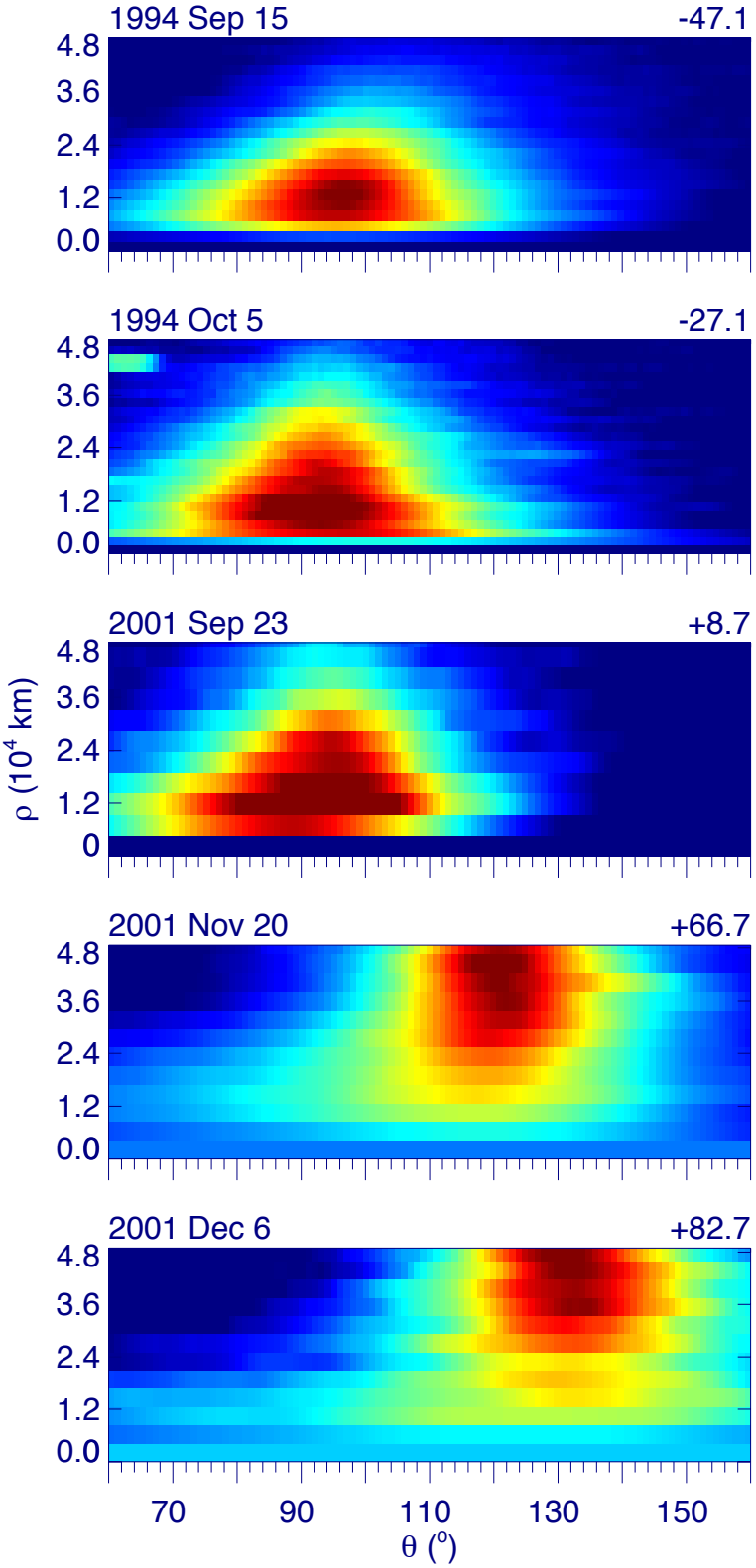
1994 Sep 15
-47.1
1994 Oct 5
-27.1
2001 Sep 23
+8.7
2001 Nov 20
+66.7
2001 Dec 6
+82.7
4.8
3.6
2.4
1.2
0.0
0
ρ (10^4 km)
70
90
110
130
150
θ (°)

Figure 9

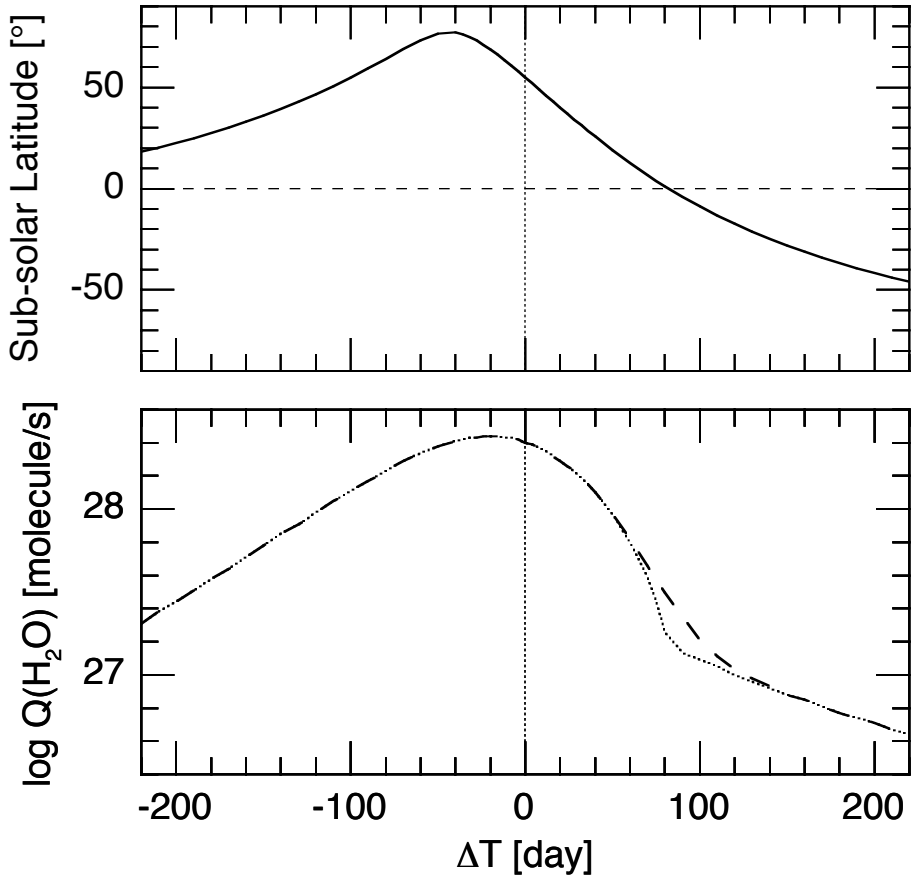
Sub-solar Latitude [°]
50
0
-50
log Q(H2O) [molecule/s]
28
27
-200
-100
0
100
200
ΔT [day]

Figure 10

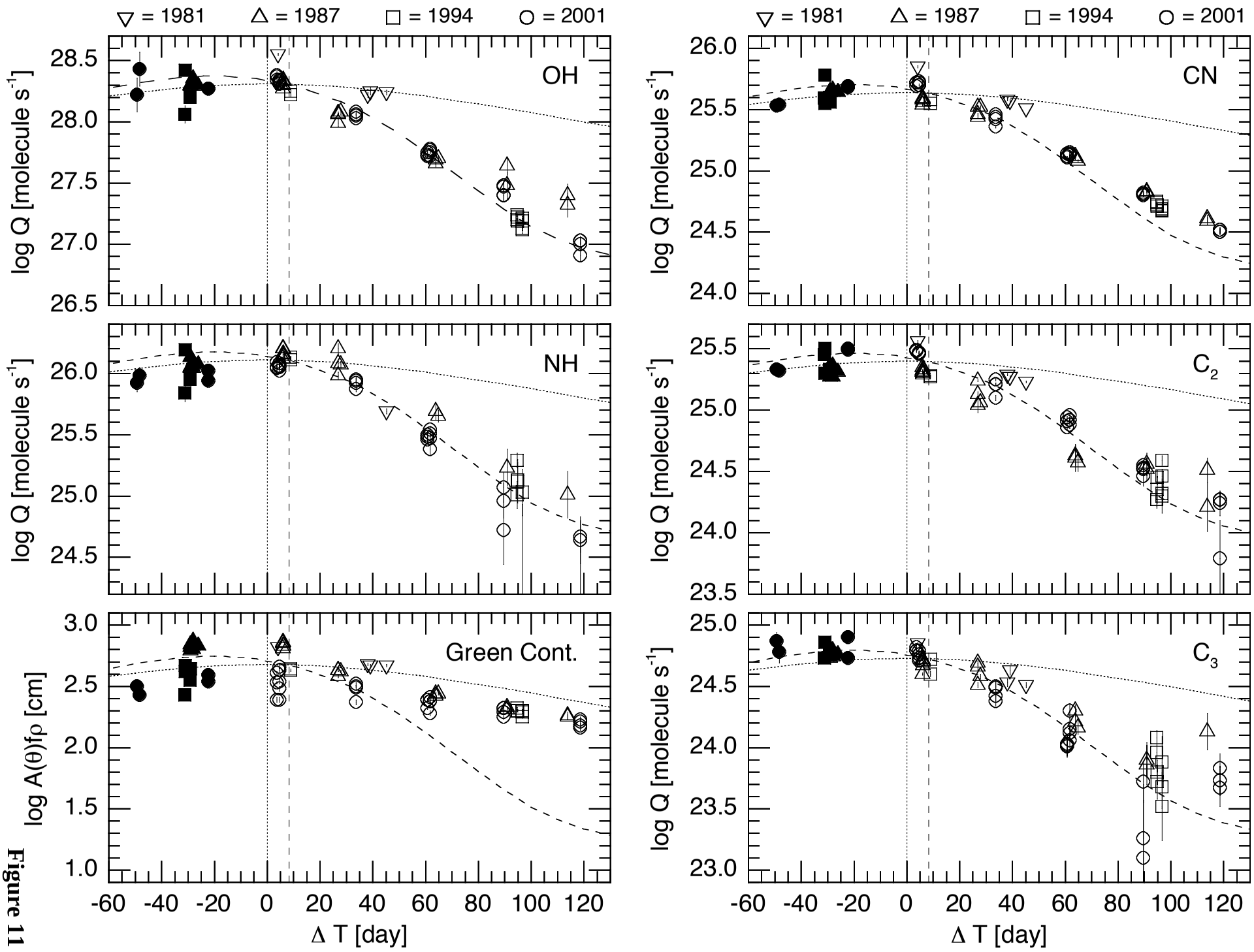
▽ = 1981
△ = 1987
□ = 1994
○ = 2001
OH
NH
Green Cont.
CN
C2
C3
log Q [molecule s-1]
log A(θ)fρ [cm]
Δ T [day]

Figure 11

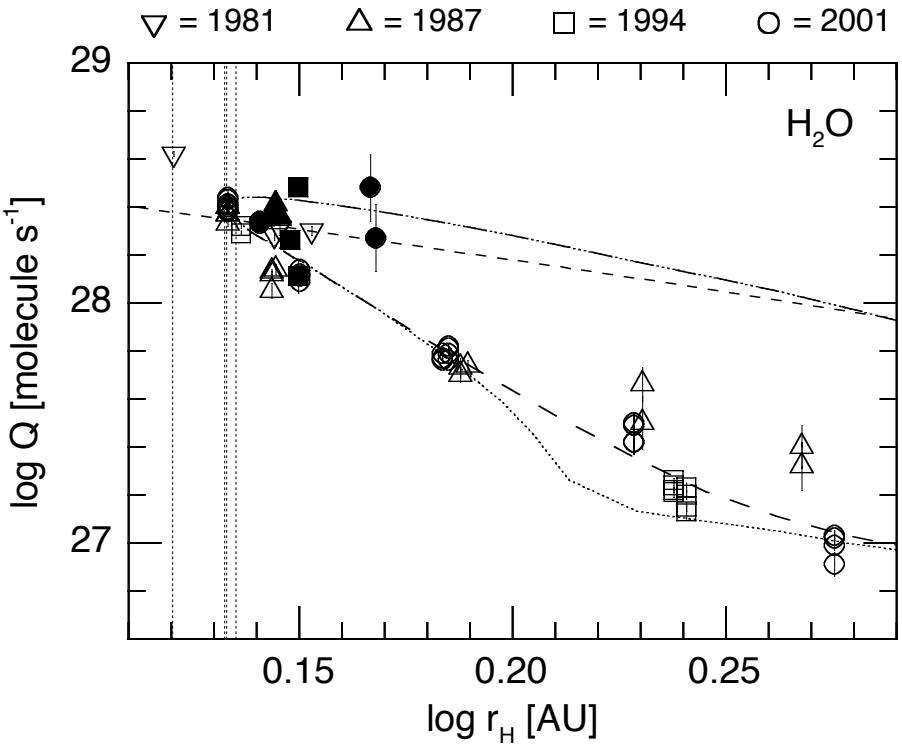
▽ = 1981
△ = 1987
□ = 1994
○ = 2001
H2O
log Q [molecule s-1]
log rH [AU]
29
28
27
0.15
0.20
0.25

Figure 12

TABLE I

CCD Observing Circumstances for Comet 19P/Borrelly

UT Date[a]	ΔT[b] (day)	r_H (AU)	Δ (AU)	Pixel Scale[c] (km/pixel)	Phase Angle (°)	Sun PA (°)
1994 Sep 14.4	–48.1	1.473	1.109	596	43	86
1994 Sep 15.4	–47.1	1.469	1.099	591	43	87
1994 Oct 4.4	–28.1	1.403	0.930	500	45	94
1994 Oct 5.4	–27.1	1.401	0.921	495	45	95
1994 Oct 7.4	–25.1	1.396	0.904	486	46	95
2001 Sep 20.5	+5.7	1.360	1.483	1220	41	100
2001 Sep 22.5	+7.7	1.361	1.475	1213	41	101
2001 Sep 23.5	+8.7	1.362	1.471	1210	41	101
2001 Nov 20.5	+66.7	1.558	1.313	1080	39	118
2001 Dec 6.5	+82.7	1.650	1.293	1063	37	116
2002 Jan 12.4	+119.6	1.893	1.287	1059	29	99
2002 Mar 19.2	+185.5	2.365	1.622	1334	20	3

[a] Mid-time of observations; all Borrelly images were obtained within an interval of about 3 hrs or less.

[b] Time from perihelion.

[c] Effective projected pixel scale after on-chip 2x2 binning.

TABLE II

Photometry Observing Circumstances and Fluorescence Efficiencies for Comet 19P/Borrelly

UT Date	ΔT (day)	r_H (AU)	Δ (AU)	Phase Angle (°)	$\dot{r}_H$ (km s^{-1})	log L/N[a] (erg s^{-1} molecule^{-1}) OH	NH	CN	Teles[b]
1981 Feb 24.14	+4.13	1.320	1.554	39.2	+0.8	–14.772	–13.291	–12.569	L42
1981 Mar 30.15	+38.14	1.394	1.762	34.5	+6.5	–14.527	–13.245	–12.327	L42
1981 Mar 31.14	+39.13	1.398	1.770	34.3	+6.7	–14.526	–13.242	–12.327	L42
1981 Apr 6.16	+45.15	1.422	1.817	33.3	+7.5	–14.526	–13.231	–12.327	L72
1987 Nov 19.27	–29.06	1.398	0.523	31.1	–4.8	–14.759	–13.136	–12.448	L42
1987 Nov 20.29	–28.05	1.395	0.519	31.1	–4.7	–14.759	–13.137	–12.450	L42
1987 Nov 22.26	–26.08	1.390	0.511	31.0	–4.4	–14.760	–13.142	–12.456	L42
1987 Dec 24.35	+6.05	1.359	0.526	36.1	+1.0	–14.807	–13.296	–12.559	M88
1988 Jan 14.27	+26.93	1.392	0.674	40.6	+4.5	–14.610	–13.283	–12.358	L42
1988 Jan 15.28	+27.95	1.395	0.683	40.7	+4.7	–14.602	–13.279	–12.352	L42
1988 Feb 20.22	+63.89	1.541	1.066	39.5	+9.1	–14.543	–13.217	–12.330	L72
1988 Feb 21.21	+64.88	1.547	1.078	39.4	+9.2	–14.539	–13.216	–12.331	L72
1988 Mar 18.22	+90.89	1.700	1.403	35.8	+11.0	–14.386	–13.208	–12.352	L72
1988 Apr 10.19	+113.86	1.853	1.713	32.3	+11.9	–14.316	–13.208	–12.380	L42
1994 Oct 1.39	–31.05	1.412	0.955	45.1	–5.1	–14.760	–13.132	–12.442	L31
1994 Oct 3.42	–29.07	1.406	0.938	45.3	–4.8	–14.759	–13.136	–12.448	L31
1994 Nov 10.39	+8.91	1.369	0.677	43.2	+1.5	–14.784	–13.306	–12.530	L31
1995 Feb 4.30	+94.80	1.729	0.944	27.0	+11.1	–14.419	–13.208	–12.355	L42
1995 Feb 6.18	+96.70	1.741	0.962	27.0	+11.2	–14.412	–13.208	–12.358	L42
2001 Jul 27.46	–49.28	1.472	1.809	34.1	–7.5	–14.784	–13.120	–12.418	L42
2001 Jul 28.45	–48.29	1.468	1.801	34.3	–7.4	–14.785	–13.120	–12.418	L42
2001 Aug 23.45	–22.29	1.383	1.627	38.2	–3.8	–14.763	–13.152	–12.469	L42
2001 Sep 18.42	+3.69	1.359	1.492	40.9	+0.6	–14.819	–13.285	–12.577	L42
2001 Sep 19.46	+4.70	1.359	1.488	41.0	+0.8	–14.814	–13.291	–12.569	L42
2001 Oct 18.44	+33.70	1.413	1.384	41.7	+5.5	–14.579	–13.262	–12.336	L42
2001 Nov 14.44	+60.70	1.526	1.323	39.8	+8.8	–14.553	–13.219	–12.330	L42
2001 Nov 15.42	+61.68	1.531	1.321	39.7	+8.9	–14.550	–13.218	–12.330	L42
2001 Dec 13.37	+89.63	1.692	1.287	35.4	+10.9	–14.435	–13.209	–12.350	L42
2002 Jan 11.40	+118.66	1.886	1.286	29.0	+12.0	–14.350	–13.208	–12.384	L42

[a] Fluorescence efficiencies are for r_H = 1 AU, and are scaled by r_H^{-2} in the reductions.

[b] Telescope ID: L72 = Lowell 72-inch (1.8-m); L42 = Lowell 42-inch (1.1-m); L31 = 31-inch (0.8-m); M88 = Mauna Kea Observatory 88-inch (2.2-m).

TABLE III

Photometric Fluxes and Aperture Abundances for Comet 19P/Borrelly

UT Date	# [a]	Aperture Size (arcsec)	Aperture log ρ (km)	log Emission Band Flux (erg cm^{-2} s^{-1}) OH	NH	CN	C_3	C_2	log Continuum Flux (erg cm^{-2} s^{-1} Å^{-1}) UV	Blue	Green	log M(ρ) (molecule) OH	NH	CN	C_3	C_2
1981 Feb 24.14	2	37.8	4.33	–10.27	—	–10.60	–10.95	–10.85	–13.45	—	–13.16	32.58	—	30.04	29.13	29.57
1981 Mar 30.15	2	37.8	4.38	–10.45	—	–10.72	–11.37	–11.22	–13.73	—	–13.40	32.31	—	29.83	28.86	29.35
1981 Mar 31.14	1	37.8	4.38	–10.42	—	–10.74	–11.28	–11.25	–13.84	—	–13.42	32.34	—	29.82	28.96	29.33
1981 Apr 6.16	1	38.9	4.41	–10.44	–11.92	–10.81	–11.41	–11.30	–13.70	—	–13.43	32.36	29.59	29.79	28.86	29.32
1987 Nov 19.26	3	75.2	4.15	–9.91	–10.78	–10.06	–10.26	–10.45	–12.81	—	–12.46	32.02	29.54	29.56	28.91	29.07
1987 Nov 19.28	4	53.4	4.01	–10.14	–11.02	–10.30	–10.48	–10.74	–12.95	—	–12.57	31.79	29.30	29.32	28.70	28.78
1987 Nov 19.28	1	37.8	3.86	–10.40	–11.20	–10.55	–10.70	–11.02	–13.08	—	–12.70	31.54	29.12	29.07	28.48	28.51
1987 Nov 20.28	2	75.2	4.15	–9.88	–10.78	–10.05	–10.27	–10.44	–12.81	—	–12.44	32.04	29.53	29.56	28.89	29.07
1987 Nov 20.26	3	53.4	4.00	–10.12	–11.00	–10.29	–10.48	–10.70	–12.93	—	–12.56	31.81	29.31	29.33	28.69	28.81
1987 Nov 20.29	2	37.8	3.85	–10.34	–11.23	–10.54	–10.68	–11.02	–13.06	—	–12.67	31.59	29.07	29.08	28.49	28.50
1987 Nov 22.26	3	53.4	4.00	–10.15	–11.00	–10.30	–10.46	–10.72	–12.93	—	–12.55	31.77	29.30	29.31	28.69	28.78
1987 Dec 24.36	2	56.8	4.03	–10.11	–11.03	–10.38	–10.46	–10.61	–12.93	—	–12.53	31.86	29.43	29.33	28.70	28.89
1987 Dec 24.42	1	40.3	3.89	–10.32	–11.26	–10.63	–10.65	–10.88	–13.07	—	–12.67	31.64	29.20	29.09	28.51	28.63
1987 Dec 24.42	1	28.5	3.74	–10.58	–11.49	–10.89	–10.86	–11.15	–13.21	—	–12.81	31.39	28.96	28.83	28.30	28.35
1987 Dec 24.35	2	20.0	3.58	–10.87	–11.73	–11.14	–11.06	–11.40	–13.34	—	–12.94	31.09	28.72	28.58	28.10	28.10
1987 Dec 24.39	1	14.2	3.43	–11.13	–11.99	–11.41	–11.33	–11.68	–13.49	—	–13.09	30.83	28.47	28.30	27.83	27.82
1987 Dec 24.35	2	10.1	3.28	–11.43	–12.31	–11.69	–11.63	–11.91	–13.64	—	–13.25	30.53	28.14	28.03	27.52	27.59
1988 Jan 14.28	1	75.2	4.26	–10.03	–10.91	–10.15	–10.48	–10.61	–13.14	—	–12.72	31.97	29.76	29.60	28.91	29.13
1988 Jan 14.24	1	37.8	3.97	–10.52	–11.52	–10.69	–10.99	–11.20	–13.45	—	–13.07	31.48	29.16	29.06	28.40	28.55
1988 Jan 14.27	1	18.8	3.66	–11.10	–11.83	–11.18	–11.25	–11.79	–13.82	—	–13.32	30.90	28.85	28.58	28.14	27.95
1988 Jan 15.28	1	37.8	3.97	–10.49	–11.43	–10.61	–10.93	–11.27	–13.42	—	–13.03	31.51	29.26	29.15	28.48	28.48
1988 Feb 20.23	1	19.5	3.88	–11.55	–12.45	–11.69	–11.83	–12.39	–14.26	—	–13.80	30.87	28.65	28.52	28.05	27.84
1988 Feb 20.20	1	13.7	3.72	–11.78	—	–11.93	–12.14	–12.66	–14.36	—	–13.94	30.64	—	28.28	27.74	27.57
1988 Feb 21.21	2	19.5	3.88	–11.51	–12.50	–11.72	–11.97	–12.45	–14.23	—	–13.80	30.92	28.61	28.50	27.92	27.79
1988 Mar 18.23	1	38.9	4.30	–11.10	–12.57	–11.69	–12.05	–12.19	–14.22	—	–13.82	31.49	28.85	28.87	28.15	28.36
1988 Mar 18.21	1	27.6	4.15	–11.50	–14.93	–11.93	–12.27	–12.39	–14.29	—	–13.95	31.09	26.48	28.63	27.93	28.16
1988 Apr 10.21	2	75.2	4.67	–10.97	–12.47	–11.68	–11.72	–12.22	–14.41	—	–13.76	31.79	29.19	29.15	28.74	28.57
1988 Apr 10.16	1	53.4	4.52	–11.28	—	–11.88	—	–12.14	–14.12	—	–13.89	31.49	—	28.95	—	28.66
1994 Oct 1.35	1	55.1	4.28	–10.49	–11.31	–10.46	–10.74	–10.70	–13.38	—	–13.22	31.98	29.53	29.69	28.96	29.35
1994 Oct 1.50	1	38.7	4.13	–10.37	–11.20	–10.51	–10.77	–10.89	–13.60	—	–13.14	32.10	29.64	29.64	28.93	29.16
1994 Oct 1.43	11	27.5	3.98	—	—	–10.97	—	–11.32	—	—	–13.33	—	—	29.18	—	28.73
1994 Oct 3.40	2	77.9	4.42	–10.10	–10.95	–10.23	–10.55	–10.59	–13.30	—	–12.94	32.35	29.88	29.91	29.14	29.45
1994 Oct 3.43	9	27.5	3.97	—	—	–10.96	—	–11.32	—	—	–13.30	—	—	29.18	—	28.72
1994 Nov 10.44	1	77.9	4.28	–9.97	–10.84	–10.22	–10.42	–10.53	–13.08	—	–12.69	32.19	29.85	29.69	28.96	29.20
1994 Nov 10.35	1	55.1	4.13	–10.24	–11.12	–10.48	–10.69	–10.77	–13.22	—	–12.84	31.93	29.57	29.43	28.69	28.96
1995 Feb 4.25	1	106.4	4.56	–10.79	–12.03	–11.06	–11.29	–11.71	–13.72	—	–13.24	31.51	29.05	29.17	28.59	28.51
1995 Feb 4.21	3	75.3	4.41	–11.06	–12.00	–11.29	–11.54	–11.94	–13.77	—	–13.37	31.23	29.09	28.94	28.33	28.28
1995 Feb 4.32	1	52.8	4.26	–11.32	–12.41	–11.54	–11.87	–12.00	–13.92	—	–13.54	30.98	28.67	28.69	28.00	28.22
1995 Feb 4.35	1	37.5	4.11	–11.54	–12.67	–11.78	–12.13	–12.34	–14.09	—	–13.69	30.76	28.41	28.45	27.74	27.88
1995 Feb 6.13	1	149.9	4.72	–10.70	—	–10.92	—	–11.20	–13.39	—	–13.15	31.61	—	29.34	—	29.04
1995 Feb 6.17	1	106.4	4.57	–10.84	—	–11.15	–11.70	–11.68	–13.65	—	–13.26	31.46	—	29.10	28.20	28.56
1995 Feb 6.19	3	75.3	4.42	–11.13	–12.26	–11.33	–11.64	–11.92	–13.77	—	–13.40	31.18	28.84	28.93	28.25	28.32
1995 Feb 6.23	2	52.8	4.27	–11.30	–13.56	–11.59	–12.17	–12.01	–13.90	—	–13.56	31.01	27.54	28.66	27.73	28.24

[a] Number of observations averaged.

TABLE III—*Continued*

Photometric Fluxes and Aperture Abundances for Comet 19P/Borrelly

UT Date	# [a]	Aperture Size (arcsec)	Aperture log ρ (km)	log Emission Band Flux (erg cm^{-2} s^{-1}) OH	NH	CN	C_3	C_2	log Continuum Flux (erg cm^{-2} s^{-1} Å^{-1}) UV	Blue	Green	log M(ρ) (molecule) OH	NH	CN	C_3	C_2
2001 Jul 27.46	1	47.3	4.49	−10.63	−11.48	−10.80	−11.01	−11.12	−14.09	−13.75	−13.55	32.45	29.94	29.92	29.29	29.52
2001 Jul 28.45	1	60.7	4.60	−10.26	−11.25	−10.64	−11.01	−10.97	−13.72	−13.52	−13.50	32.82	30.17	30.07	29.28	29.67
2001 Aug 23.45	1	94.6	4.75	−10.04	−10.93	−10.20	−10.85	−10.46	−13.44	−13.19	−13.11	32.88	30.37	30.42	29.31	30.04
2001 Aug 23.44	1	60.7	4.55	−10.30	−11.14	−10.45	−10.79	−10.71	−13.83	−13.28	−13.25	32.62	30.16	30.17	29.36	29.79
2001 Sep 18.41	1	151.8	4.91	−9.69	−10.64	−10.00	−10.64	−10.20	−13.34	−13.06	−13.00	33.19	30.71	30.64	29.42	30.21
2001 Sep 18.43	2	94.6	4.71	−9.95	−10.91	−10.23	−10.70	−10.43	−13.50	−13.07	−13.06	32.93	30.44	30.41	29.37	29.98
2001 Sep 18.43	1	60.7	4.52	−10.24	−11.17	−10.50	−10.85	−10.67	−13.64	−13.20	−13.18	32.64	30.18	30.14	29.22	29.74
2001 Sep 19.45	1	199.1	5.03	−9.60	−10.52	−9.87	−10.67	−10.11	−13.25	−12.94	−12.88	33.27	30.83	30.76	29.40	30.30
2001 Sep 19.43	1	151.8	4.91	−9.72	−10.63	−10.00	−10.72	−10.22	−13.22	−12.97	−12.91	33.16	30.72	30.63	29.34	30.19
2001 Sep 19.42	1	94.6	4.71	−10.00	−10.92	−10.24	−10.73	−10.44	−13.45	−13.09	−13.05	32.87	30.43	30.38	29.33	29.96
2001 Sep 19.44	1	60.7	4.52	−10.25	−11.20	−10.49	−10.87	−10.69	−13.59	−13.20	−13.16	32.62	30.16	30.14	29.19	29.71
2001 Sep 19.46	1	37.5	4.31	−10.57	−11.52	−10.78	−11.05	−10.98	−13.74	−13.36	−13.33	32.31	29.84	29.85	29.01	29.42
2001 Oct 18.42	1	151.8	4.88	−9.75	−10.77	−10.02	−10.90	−10.44	−13.42	−13.01	−13.01	32.86	30.53	30.35	29.14	29.94
2001 Oct 18.43	1	94.6	4.68	−10.04	−11.03	−10.28	−10.99	−10.72	−13.58	−13.14	−13.10	32.57	30.27	30.09	29.04	29.66
2001 Oct 18.45	1	60.7	4.48	−10.33	−11.40	−10.56	−11.24	−10.97	−13.62	−13.30	−13.26	32.28	29.89	29.80	28.79	29.40
2001 Oct 18.46	1	37.5	4.27	−10.66	−11.67	−10.92	−11.38	−11.38	−13.95	−13.58	−13.51	31.95	29.62	29.45	28.65	29.00
2001 Nov 14.43	1	151.8	4.86	−10.13	−11.26	−10.39	−11.38	−10.80	−13.37	−13.13	−13.11	32.49	30.02	29.99	28.68	29.60
2001 Nov 14.44	1	94.6	4.66	−10.43	−11.52	−10.68	−11.48	−11.14	−13.74	−13.30	−13.25	32.18	29.75	29.71	28.58	29.27
2001 Nov 14.45	1	60.7	4.46	−10.72	−11.84	−10.95	−11.62	−11.35	−13.82	−13.50	−13.44	31.90	29.44	29.44	28.44	29.05
2001 Nov 15.41	1	151.8	4.86	−10.13	−11.19	−10.39	−11.23	−10.79	−13.53	−13.15	−13.16	32.48	30.09	30.00	28.83	29.62
2001 Nov 15.42	1	94.6	4.66	−10.38	−11.51	−10.66	−11.21	−11.08	−13.81	−13.31	−13.26	32.23	29.77	29.73	28.85	29.33
2001 Nov 15.43	1	60.7	4.46	−10.72	−11.95	−10.92	−11.60	−11.35	−13.78	−13.48	−13.45	31.89	29.33	29.47	28.47	29.06
2001 Nov 15.44	1	37.5	4.25	−11.00	−12.20	−11.23	−11.73	−11.70	−14.08	−13.67	−13.64	31.61	29.08	29.16	28.33	28.71
2001 Dec 13.36	1	151.8	4.85	−10.40	−11.88	−10.84	—	−11.31	−13.59	−13.27	−13.26	32.16	29.46	29.64	—	29.16
2001 Dec 13.37	1	94.6	4.64	−10.68	−12.07	−11.12	−12.29	−11.56	−13.78	−13.47	−13.43	31.88	29.26	29.36	27.83	28.91
2001 Dec 13.38	1	60.7	4.45	−11.05	—	−11.39	−12.61	−11.87	−13.91	−13.68	−13.59	31.51	—	29.09	27.51	28.61
2001 Dec 13.39	1	37.5	4.24	−11.39	−13.08	−11.70	−12.22	−12.25	−14.17	−13.83	−13.80	31.17	28.25	28.77	27.91	28.22
2002 Jan 11.38	1	151.8	4.85	−10.88	−12.30	−11.31	−11.80	−11.69	−13.92	−13.51	−13.45	31.69	29.12	29.29	28.42	28.88
2002 Jan 11.40	2	94.6	4.64	−11.22	−13.18	−11.57	−11.80	−11.98	−14.10	−13.67	−13.63	31.35	28.25	29.03	28.42	28.59
2002 Jan 11.40	1	60.7	4.45	−11.49	−12.97	−11.85	−12.08	−12.29	−14.34	−13.87	−13.80	31.08	28.46	28.75	28.14	28.28
2002 Jan 11.42	1	37.5	4.24	−11.95	—	−12.20	—	−13.07	−14.40	−14.04	−13.98	30.62	—	28.40	—	27.49

[a] Number of observations averaged.

TABLE IV

Photometric Production Rates for Comet 19P/Borrelly

UT Date	ΔT (day)	log r_H (AU)	# [a]	log ρ (km)	log Q [b] (molecule s^{-1}) OH	NH	CN	C_3	C_2	log $A(\theta)f\rho$ [b] (cm) UV	Blue	Green	log Q H_2O
1981 Feb 24.14	4.13	0.121	2	4.33	28.55 .01	—	25.85 .01	24.85 .01	25.56 .01	2.72 .02	—	2.82 .01	28.62
1981 Mar 30.15	38.14	0.144	2	4.38	28.22 .02	—	25.58 .01	24.53 .03	25.29 .01	2.55 .04	—	2.68 .01	28.28
1981 Mar 31.14	39.13	0.146	1	4.38	28.25 .03	—	25.57 .01	24.63 .04	25.27 .01	2.44 .06	—	2.67 .01	28.31
1981 Apr 6.16	45.15	0.153	1	4.41	28.24 .02	25.69 .02	25.51 .00	24.51 .02	25.23 .01	2.59 .02	—	2.67 .01	28.30
1987 Nov 19.26	–29.07	0.146	3	4.15	28.29 .01	26.04 .01	25.65 .00	24.81 .01	25.36 .01	2.66 .01	—	2.79 .00	28.35
1987 Nov 19.28	–29.06	0.146	4	4.01	28.30 .01	26.05 .01	25.64 .00	24.76 .01	25.31 .01	2.68 .01	—	2.82 .00	28.36
1987 Nov 19.28	–29.05	0.146	1	3.86	28.30 .02	26.13 .02	25.64 .00	24.73 .02	25.27 .02	2.70 .01	—	2.84 .00	28.36
1987 Nov 20.28	–28.05	0.145	2	4.15	28.32 .01	26.04 .01	25.66 .00	24.79 .01	25.36 .01	2.66 .01	—	2.80 .00	28.38
1987 Nov 20.26	–28.06	0.145	3	4.00	28.32 .01	26.07 .01	25.65 .00	24.75 .01	25.34 .01	2.70 .01	—	2.83 .00	28.38
1987 Nov 20.29	–28.04	0.145	2	3.85	28.35 .02	26.09 .02	25.64 .00	24.74 .01	25.27 .01	2.71 .01	—	2.87 .00	28.41
1987 Nov 22.26	–26.08	0.143	3	4.00	28.29 .01	26.07 .01	25.64 .00	24.76 .01	25.31 .01	2.68 .01	—	2.83 .00	28.35
1987 Dec 24.36	6.03	0.133	2	4.03	28.30 .00	26.12 .00	25.59 .00	24.72 .00	25.35 .00	2.65 .01	—	2.81 .00	28.37
1987 Dec 24.42	6.09	0.133	1	3.89	28.34 .00	26.14 .01	25.59 .00	24.71 .00	25.33 .00	2.66 .01	—	2.83 .00	28.40
1987 Dec 24.42	6.09	0.133	1	3.74	28.33 .00	26.16 .01	25.58 .00	24.70 .01	25.30 .01	2.67 .01	—	2.83 .00	28.40
1987 Dec 24.35	6.02	0.133	2	3.58	28.30 .00	26.20 .01	25.58 .00	24.72 .01	25.31 .01	2.69 .01	—	2.86 .00	28.37
1987 Dec 24.39	6.06	0.133	1	3.43	28.30 .01	26.20 .02	25.56 .00	24.67 .01	25.29 .02	2.69 .01	—	2.86 .00	28.37
1987 Dec 24.35	6.02	0.133	2	3.28	28.27 .01	26.15 .02	25.54 .01	24.60 .01	25.32 .01	2.69 .01	—	2.85 .00	28.33
1988 Jan 14.28	26.95	0.144	1	4.26	28.07 .01	26.08 .02	25.52 .00	24.69 .02	25.24 .01	2.44 .02	—	2.63 .00	28.13
1988 Jan 14.24	26.91	0.144	1	3.97	28.06 .01	25.98 .03	25.44 .01	24.51 .02	25.13 .02	2.43 .02	—	2.58 .01	28.12
1988 Jan 14.27	26.94	0.144	1	3.66	27.99 .03	26.20 .04	25.46 .01	24.66 .03	25.04 .06	2.36 .03	—	2.63 .01	28.05
1988 Jan 15.28	27.95	0.145	1	3.97	28.08 .02	26.07 .03	25.52 .01	24.58 .02	25.06 .03	2.48 .02	—	2.62 .01	28.14
1988 Feb 20.23	63.90	0.188	1	3.88	27.66 .03	25.69 .07	25.10 .01	24.30 .05	24.63 .08	2.20 .03	—	2.42 .01	27.70
1988 Feb 20.20	63.87	0.188	1	3.72	27.69 .04	—	25.12 .01	24.21 .07	24.61 .11	2.26 .03	—	2.44 .01	27.73
1988 Feb 21.21	64.88	0.189	2	3.88	27.70 .02	25.65 .05	25.08 .01	24.16 .05	24.57 .07	2.24 .02	—	2.44 .01	27.74
1988 Mar 18.23	90.90	0.230	1	4.30	27.64 .07	25.23 .15	24.83 .01	23.90 .14	24.52 .09	2.14 .06	—	2.31 .01	27.66
1988 Mar 18.21	90.88	0.230	1	4.15	27.48 .11	23.12 .99	24.82 .02	23.86 .16	24.56 .09	2.22 .05	—	2.33 .01	27.50
1988 Apr 10.21	113.88	0.268	2	4.67	27.40 .09	25.01 .19	24.59 .03	24.13 .15	24.21 .20	1.83 .15	—	2.25 .02	27.40
1988 Apr 10.16	113.83	0.268	1	4.52	27.32 .10	—	24.61 .03	—	24.51 .10	2.27 .08	—	2.26 .03	27.32
1994 Oct 1.35	–31.13	0.150	1	4.28	28.06 .07	25.84 .07	25.59 .01	24.73 .03	25.45 .01	2.51 .04	—	2.43 .01	28.11
1994 Oct 1.50	–30.98	0.150	1	4.13	28.42 .01	26.19 .04	25.78 .01	24.86 .03	25.50 .02	2.44 .04	—	2.67 .01	28.48
1994 Oct 1.43	–31.05	0.150	11	3.98	—	—	25.55 .00	—	25.30 .01	—	—	2.62 .00	—
1994 Oct 3.40	–29.08	0.148	2	4.42	28.20 .03	25.95 .03	25.60 .00	24.77 .02	25.33 .01	2.42 .03	—	2.55 .01	28.26
1994 Oct 3.43	–29.06	0.148	9	3.97	—	—	25.56 .00	—	25.30 .01	—	—	2.64 .00	—
1994 Nov 10.44	8.96	0.136	1	4.28	28.25 .01	26.13 .01	25.58 .00	24.72 .01	25.28 .01	2.48 .01	—	2.64 .00	28.32
1994 Nov 10.35	8.87	0.136	1	4.13	28.22 .01	26.11 .02	25.55 .00	24.60 .02	25.27 .01	2.49 .01	—	2.63 .01	28.29
1995 Feb 4.25	94.77	0.238	1	4.56	27.24 .01	25.01 .11	24.75 .01	24.08 .06	24.27 .07	2.05 .04	—	2.30 .01	27.26
1995 Feb 4.21	94.72	0.238	3	4.41	27.20 .01	25.29 .06	24.74 .01	23.96 .05	24.27 .06	2.15 .03	—	2.32 .01	27.22
1995 Feb 4.32	94.84	0.238	1	4.26	27.19 .02	25.13 .14	24.72 .01	23.80 .10	24.45 .06	2.16 .04	—	2.30 .01	27.21
1995 Feb 4.35	94.87	0.238	1	4.11	27.22 .02	25.12 .18	24.71 .02	23.72 .14	24.35 .11	2.14 .04	—	2.30 .01	27.24
1995 Feb 6.13	96.65	0.241	1	4.72	27.12 .03	—	24.69 .01	—	24.59 .04	2.25 .05	—	2.25 .01	27.13
1995 Feb 6.17	96.69	0.241	1	4.57	27.19 .02	—	24.67 .01	23.68 .18	24.32 .09	2.13 .05	—	2.29 .01	27.20
1995 Feb 6.19	96.71	0.241	3	4.42	27.13 .02	25.03 .19	24.71 .01	23.88 .21	24.30 .14	2.17 .03	—	2.30 .01	27.15
1995 Feb 6.23	96.75	0.241	2	4.27	27.21 .02	23.99 .94	24.68 .01	23.52 .28	24.46 .06	2.19 .03	—	2.30 .01	27.23

[a] Number of observations averaged.

[b] Production rates, followed by uncertainties.

TABLE IV—*Continued*

Photometric Production Rates for Comet 19P/Borrelly

UT Date	ΔT (day)	log r_H (AU)	# [a]	log ρ (km)	log Q [b] (molecule s^{-1}) OH	NH	CN	C_3	C_2	log $A(\theta)f\rho$ [b] (cm) UV	Blue	Green	log Q H_2O
2001 Jul 27.46	−49.28	0.168	1	4.49	28.22 .14	25.92 .07	25.53 .02	24.87 .07	25.33 .02	2.26 .25	2.27 .07	2.50 .03	28.27
2001 Jul 28.45	−48.29	0.167	1	4.60	28.43 .14	25.98 .07	25.54 .02	24.78 .09	25.32 .02	2.52 .20	2.39 .06	2.43 .04	28.48
2001 Aug 23.45	−22.29	0.141	1	4.75	28.27 .02	25.94 .02	25.69 .00	24.73 .05	25.50 .01	2.51 .07	2.44 .03	2.54 .02	28.33
2001 Aug 23.44	−22.30	0.141	1	4.55	28.27 .04	26.02 .03	25.68 .01	24.90 .04	25.49 .01	2.32 .12	2.54 .03	2.59 .02	28.34
2001 Sep 18.41	3.67	0.133	1	4.91	28.38 .03	26.04 .02	25.72 .00	24.79 .06	25.49 .01	2.35 .10	2.30 .04	2.39 .02	28.44
2001 Sep 18.43	3.69	0.133	2	4.71	28.37 .01	26.05 .01	25.72 .00	24.82 .02	25.48 .01	2.40 .04	2.50 .01	2.53 .01	28.43
2001 Sep 18.43	3.69	0.133	1	4.52	28.34 .02	26.09 .02	25.69 .00	24.79 .03	25.49 .01	2.45 .05	2.56 .02	2.61 .01	28.41
2001 Sep 19.45	4.71	0.133	1	5.03	28.32 .01	26.02 .01	25.73 .00	24.73 .05	25.47 .01	2.32 .06	2.31 .03	2.39 .02	28.39
2001 Sep 19.43	4.69	0.133	1	4.91	28.34 .01	26.06 .02	25.72 .00	24.71 .05	25.47 .01	2.48 .06	2.39 .03	2.48 .02	28.41
2001 Sep 19.42	4.68	0.133	1	4.71	28.31 .02	26.05 .02	25.70 .00	24.79 .04	25.46 .01	2.45 .07	2.48 .02	2.54 .02	28.38
2001 Sep 19.44	4.70	0.133	1	4.52	28.33 .01	26.06 .02	25.70 .00	24.76 .03	25.46 .01	2.50 .05	2.56 .02	2.63 .02	28.40
2001 Sep 19.46	4.72	0.133	1	4.31	28.32 .02	26.08 .02	25.70 .01	24.76 .03	25.47 .01	2.56 .04	2.61 .02	2.66 .02	28.39
2001 Oct 18.42	33.68	0.150	1	4.88	28.08 .01	25.92 .02	25.46 .00	24.49 .06	25.25 .01	2.28 .07	2.36 .02	2.37 .02	28.14
2001 Oct 18.43	33.69	0.150	1	4.68	28.06 .01	25.95 .02	25.44 .00	24.50 .05	25.21 .01	2.32 .06	2.43 .02	2.50 .01	28.12
2001 Oct 18.45	33.71	0.150	1	4.48	28.05 .01	25.87 .02	25.42 .00	24.38 .04	25.21 .01	2.47 .04	2.47 .02	2.52 .01	28.11
2001 Oct 18.46	33.72	0.150	1	4.27	28.03 .01	25.94 .02	25.36 .01	24.42 .04	25.10 .02	2.35 .05	2.40 .02	2.49 .02	28.09
2001 Nov 14.43	60.69	0.184	1	4.86	27.75 .01	25.46 .03	25.14 .00	24.01 .09	24.94 .01	2.38 .05	2.28 .02	2.32 .01	27.79
2001 Nov 14.44	60.70	0.184	1	4.66	27.73 .01	25.50 .03	25.12 .00	24.02 .09	24.86 .02	2.21 .06	2.32 .02	2.39 .01	27.77
2001 Nov 14.45	60.71	0.184	1	4.46	27.72 .01	25.48 .04	25.11 .01	24.03 .07	24.91 .02	2.32 .05	2.32 .02	2.39 .01	27.76
2001 Nov 15.41	61.67	0.185	1	4.86	27.75 .01	25.54 .03	25.15 .00	24.15 .09	24.96 .01	2.21 .07	2.26 .02	2.28 .02	27.79
2001 Nov 15.42	61.68	0.185	1	4.66	27.78 .01	25.51 .03	25.13 .01	24.30 .06	24.92 .02	2.14 .07	2.31 .02	2.38 .01	27.82
2001 Nov 15.43	61.69	0.185	1	4.46	27.72 .01	25.38 .05	25.14 .01	24.06 .06	24.92 .02	2.36 .04	2.33 .02	2.38 .01	27.76
2001 Nov 15.44	61.70	0.185	1	4.25	27.77 .02	25.47 .05	25.13 .01	24.12 .06	24.88 .03	2.27 .05	2.35 .02	2.41 .02	27.81
2001 Dec 13.36	89.62	0.228	1	4.85	27.47 .05	24.96 .14	24.82 .01	—	24.53 .04	2.23 .11	2.22 .03	2.25 .02	27.49
2001 Dec 13.37	89.63	0.228	1	4.64	27.48 .04	25.07 .12	24.80 .01	23.26 .44	24.55 .04	2.25 .10	2.22 .03	2.29 .02	27.50
2001 Dec 13.38	89.64	0.228	1	4.45	27.40 .05	—	24.81 .01	23.10 .47	24.52 .05	2.31 .07	2.21 .03	2.32 .02	27.42
2001 Dec 13.39	89.65	0.228	1	4.24	27.40 .05	24.72 .28	24.81 .02	23.72 .17	24.46 .08	2.26 .08	2.27 .02	2.32 .02	27.42
2002 Jan 11.38	118.64	0.276	1	4.85	27.03 .02	24.67 .13	24.50 .01	23.67 .15	24.27 .06	1.99 .08	2.07 .03	2.16 .02	27.03
2002 Jan 11.40	118.66	0.276	2	4.64	27.00 .02	24.12 .51	24.52 .01	23.83 .12	24.27 .06	2.02 .06	2.12 .02	2.18 .02	26.99
2002 Jan 11.40	118.66	0.276	1	4.45	27.03 .03	24.64 .19	24.52 .02	23.73 .12	24.24 .10	1.97 .08	2.12 .03	2.21 .02	27.02
2002 Jan 11.42	118.68	0.276	1	4.24	26.91 .05	—	24.50 .02	—	23.79 .31	2.12 .06	2.15 .03	2.23 .02	26.91

[a] Number of observations averaged.

[b] Production rates, followed by uncertainties.

TABLE V

Heliocentric Distance Dependencies[a] and Abundance Ratios for Comet 19P/Borrelly

Species	r_H–dependence[a]	log Production Rate Ratios (X/OH)
OH	–8.94±.29	0.00
NH	–10.58±.44	–2.28±.34
CN	–8.11±.17	–2.62±.09
C_3	–8.15±.62	–3.55±.19
C_2	–8.62±.35	–2.91±.12
UV Cont.	–3.27±.29	–25.53±.31[b]
Blue Cont.	–2.43±.27	–25.53±.36[b]
Green Cont.	–3.18±.29	–25.40±.31[b]

[a] For post-perihelion data, excluding the 1981 apparition.

[b] For the dust continuum, the ratio of $A(\theta)f\rho$ to Q(OH) has units of cm sec mol^{-1}.

TABLE VI

Measured Position Angles for the Polar Jet in Comet 19P/Borrelly

UT Date	ΔT (day)	# of Obs.	$PA^{a}_{x\text{-}y}$ (°)	$PA^{a}_{\theta-\rho}$ (°)	PA^{a}_{jet} (°)	$PA^{a}_{94/01}$ (°)	Sub-Solar Latitude (°)	Sub-Earth Latitude (°)
1994 Sep 14.4	–48.08	3	97.7	97.6	98	100	+77	+39
1994 Sep 15.4	–47.06	1	99.0	98.0	98	100	+77	+38
1994 Oct 4.4	–28.10	2	95.0	94.1	95	96	+72	+27
1994 Oct 5.4	–27.10	4	95.0	94.3	95	95	+72	+26
1994 Oct 7.4	–25.05	3	95.0	93.5	94	95	+71	+25
2001 Sep 20.5	+5.73	2	93.0	93.3	93	93	+50	+9
2001 Sep 22.5	+7.73	6	94.6	93.8	94	93	+48	+8
2001 Sep 23.5	+8.73	7	94.3	93.9	94	94	+47	+7
2001 Nov 20.5	+66.74	6	120.5	119.9	120	120	+8	–31
2001 Dec 6.5	+82.68	5	131.5	132.2	132	132	–1	–37
2002 Jan 12.4	+119.6	—[b]	—	—	—	152	–17	–37
2002 Mar 19.2	+185.5	—[b]	—	—	—	143	–38	–24

[a] Position angles: $PA_{x\text{-}y}$. is measured from *x*-*y* figures, $PA_{\theta-\rho}$ is measured from unwrapped profiles in θ, PA_{jet} is the average of $PA_{x\text{-}y}$. and $PA_{\theta-\rho}$ for each night, and $PA_{94/01}$ is the predicted position angle using the pole orientation for the 1994 and 2001 apparitions (see Table VIII).

[b] The remnant of the polar jet is no longer radial and is too diffuse to measure.

TABLE VII

Previously Published Position Angles for the Sunward Jet in Comet 19P/Borrelly

UT	Date		ΔT (day)	PA^{a}_{jet} (°)	$PA^{b}_{11/32}$ (°)	$PA^{b}_{94/01}$ (°)	Sub-Solar Latitude (°)
1911	Nov	14.0	−34.5	140[1]	145	150	+76
	Dec	9.8	−8.7	70[2]	80	139	+58
	Dec	14.8	−3.7	62[2]	58	120	+54
	Dec	14.9	−3.6	60[2]	58	119	+54
	Dec	15.8	−2.7	65[2]	55	113	+54
1912	Jan	13.9	+26.4	50[3]	15	21	+32
	Jan	19.8	+32.3	20[1]	16	22	+28
1918	Sep	1.4	−76.7	95[1]	108	118	+75
	Oct	7.3	−40.8	90[1]	94	104	+80
	Oct	13.4	−34.7	90[1]	93	102	+76
	Oct	14.4	−33.7	90[1]	92	101	+76
	Oct	17.4	−30.7	95[1]	92	100	+74
	Nov	11.2	−5.9	100[1]	84	93	+56
	Nov	25.2	+8.1	85[1]	80	88	+46
1919	Jan	4.2	+48.1	50[1]	68	73	+17
1925	Aug	18.4	−50.1	90[1]	85	95	+84
	Aug	21.4	−47.1	88[1]	84	94	+83
	Sep	16.4	−21.1	82[1]	83	92	+67
	Sep	29.4	−8.1	71[1]	84	92	+58
	Dec	24.4	+77.9	120[1]	125	131	−1
1932	Aug	12.4	−14.9	100[1]	77	87	+63
1994	Oct	20.52	−11.98	90.0	—	93	+63
	Nov	6.16	+4.66	95.0	—	94	+51
	Nov	30.07	+28.57	102.0	—	100	+33
	Nov	30.99	+29.49	101.5	—	100	+32
	Dec	3.11	+31.61	102.5	—	102	+31
	Dec	4.13	+32.63	105.0	—	102	+30
	Dec	7.23	+35.72	104.0	—	103	+28
	Dec	15.20	+43.70	108.0	—	107	+22
	Dec	23.89	+52.39	109.0	—	111	+17
	Dec	26.90	+55.40	110.0	—	112	+15
1995	Jan	2.85	+62.35	110.0	—	114	+11
	Jan	8.01	+67.51	110.0	—	114	+7
	Jan	8.79	+68.29	109.0	—	114	+7
	Jan	29.03	+88.53	111.0	—	111	−4
	Feb	1.17	+91.67	110.5	—	110	−5
	Feb	2.91	+93.41	110.0	—	110	−6
	Feb	2.95	+93.45	110.0	—	110	−6
	Feb	3.07	+93.57	110.0	—	110	−6
	Feb	5.96	+96.46	110.0	—	109	−8
	Mar	11.08	+129.58	120.0	—	101	−22

[a] Measured position angle of the "sunward" jet. Superscripts refer to the categories discussed in the text.

[b] Predicted position angles using the pole orientation for the 1911-1932 apparitions and for the 1994 and 2001 apparitions (see Table VIII).

TABLE VIII

Pole Solutions for Comet 19P/Borrelly

Apparitions	Obliquity of the Pole (°)	Orbital Longitude of the Pole (°)	RA (°)	Dec (°)
1911–1932	96±2	142±2	217	+2
1994–2001	102.7±0.5	146±1	214.1	–5.7